Article

Mesoporous Silica Nanoparticle-Supported Lipid Bilayers (Protocells) for Active Targeting and Delivery to Individual Leukemia Cells

Paul N. Durfee, Yu-Shen Lin, Darren R. Dunphy, Ayse J. Muniz, Kimberly S. Butler, Kevin R. Humphrey, Amanda J. Lokke, Jacob Ongudi Agola, Stanley S. Chou, I-Ming Chen, Walker Wharton, Jason L Townson, Cheryl L. Willman, and C. Jeffrey Brinker

ACS Nano, **Just Accepted Manuscript** • DOI: 10.1021/acsnano.6b02819 • Publication Date (Web): 15 Jul 2016

Mesoporous Silica Nanoparticle-Supported Lipid Bilayers (Protocells) for Active Targeting and Delivery to Individual Leukemia Cells

Paul N. Durfee,[†,§] Yu-Shen Lin, [‡,◆,*] Darren R. Dunphy,[§] Ayşe J. Muñiz,[¶] Kimberly S. Butler,[§] Kevin R. Humphrey,[#] Amanda J. Lokke,[¶] Jacob O. Agola,[§] Stanley S. Chou,[■] I-Ming Chen,[ǁ,Δ] Walker Wharton,[ǁ,Δ] Jason L. Townson,[‡,◆] Cheryl L. Willman,[ǁ,Δ] and C. Jeffrey Brinker[†,§,■,Δ,*]

[†] University of New Mexico, Chemical and Biological Engineering, 210 University Blvd, NE, Albuquerque, NM, USA 87131-0001

[§] University of New Mexico, Center for Micro-Engineered Materials, Advanced Materials Laboratory, MSC 04 2790, 1001 University Blvd SE, Suite 103, Albuquerque, NM, USA 87106

[‡] University of New Mexico, Internal Medicine, MSC10 5550, 1 University of New Mexico, Albuquerque, NM, USA 87131

[◆] Oncothyreon Inc, 2601 Fourth Avenue, Seattle, WA, USA 98121-3222

[¶] University of New Mexico Health Sciences Center, Biochemistry and Molecular Biology, MSC 08 4670, 1 University of New Mexico, Albuquerque, NM, USA 87131-5001

[#] Vanderbilt University, Biomedical Engineering, 2301 Vanderbilt Place, Nashville, TN, USA 37235-1826

▪ Sandia National Laboratories, Advanced Materials Laboratory, 1001 University Blvd. SE, Suite 100, Albuquerque, NM, USA 87106

[‖] University of New Mexico Department of Pathology, MSC08 4640, 1 University of New Mexico, Albuquerque, NM, USA 87131-0001

[Δ] The University of New Mexico Comprehensive Cancer Center, MSC07-4025, 1 University of New Mexico, 1201 Camino de Salud NE, Albuquerque, NM, USA 87131-0001

KEYWORDS. Mesoporous Silica Nanoparticle; Supported Lipid Bilayer; Colloidal Stability; Chorioallantoic Membrane; Leukemia Cell Targeting

ABSTRACT: Many nanocarrier cancer therapeutics currently under development, as well as those used in the clinical setting, rely upon the enhanced permeability and retention (EPR) effect to passively accumulate in the tumor microenvironment and kill cancer cells. In leukemia, where leukemogenic stem cells and their progeny circulate within the peripheral blood or bone marrow, the EPR effect may not be operative. Thus, for leukemia therapeutics, it is essential to target and bind individual circulating cells. Here, we investigate mesoporous silica nanoparticle (MSN)-supported lipid bilayers (protocells), an emerging class of nanocarriers, and establish the synthesis conditions and lipid bilayer composition needed to achieve highly monodisperse protocells that remain stable in complex media as assessed *in vitro* by dynamic light scattering and cryo-electron microscopy and *ex ovo* by direct imaging within a chick chorioallantoic

membrane (CAM) model. We show that for vesicle fusion conditions where the lipid surface area exceeds the external surface area of the MSN and the ionic strength exceeds 20 mM, we form monosized protocells (polydispersity index < 0.1) on MSN cores with varying size, shape, and pore size, whose conformal zwitterionic supported lipid bilayer confers excellent stability as judged by circulation in the CAM and minimal opsonization *in vivo* in a mouse model. Having established protocell formulations that are stable colloids, we further modified them with anti-EGFR antibodies as targeting agents and re-verified their monodispersity and stability. Then using intravital imaging in the CAM we directly observed in real time the progression of selective targeting of individual leukemia cells (using the established REH leukemia cell line transduced with EGFR) and delivery of a model cargo. Overall we have established the effectiveness of the protocell platform for individual cell targeting and delivery needed for leukemia and other disseminated disease.

It is now widely recognized that nanoparticle based drug delivery provides a new ability to package poorly soluble and/or highly toxic drugs, protect drugs and molecular cargos from enzymatic degradation, and enhance their circulation and biodistribution compared to free drug. Furthermore 'passive' or 'active' targeted delivery promises precise administration of therapeutic cargos to specific cells or tissues, while sparing collateral damage to healthy cells and tissues and potentially overcoming multiple drug resistance mechanisms.[1-3] So-called passive targeting occurs through the enhanced permeability and retention (EPR) effect resulting from 200 – 2000 nm fenestrations in the tumor vasculature that are permeable to blood components including nanoparticles.[1] Nanoparticles are retained because the lymphatic function of the tumor may be

defective and does not support convective flow back into the interstitial fluid,[4] and because diffusion of nanoparticles may be highly limited due to their dimensions.[5] Arguably all nanoparticle therapeutics smaller than several micrometers could accumulate in tumor microenvironments according to the EPR effect; but their efficiency is strongly dependent on physicochemical factors such as size, shape, surface charge, and hydrophobicity, which control colloidal stability, and accordingly circulation time, non-specific binding, opsonization, and uptake by the mononuclear phagocyte system (MPS).[1, 6] Active targeting relies on modifying the nanocarrier with ligands that bind to receptors that are over expressed or uniquely expressed on targeted cancer cells *versus* normal cells.[7] Typically active targeting also relies upon the EPR effect, and its efficiency is governed by the same physicochemical factors as those for passive targeting.[8, 9] The difference is that targeting ligands can enhance binding and, therefore, retention by the targeted cell and can often promote internalization *via* receptor-mediated endocytotic pathways.[1, 8] Targeting ligands, however, increase size, complexity, and cost and potentially alter the same physicochemical parameters that govern the EPR effect, requiring re-optimization of the surface chemistry.[1] For this reason the benefits of active targeting are often not clear-cut, and consequently considerably fewer actively targeted nanoparticle therapeutics are used clinically.[10, 11] A major exception is targeted delivery to individual or small groups of cells or circulating cells, where by definition the EPR effect is likely inoperative. Here, nanoparticle delivery to leukemias is an important case in point. Because conventional anticancer drugs used for leukemia therapy are systemic and non-targeted, they may result in significant acute and long term toxic side effects to normal tissues. Thus, there is a critical need to increase the efficacy and reduce toxicity of therapeutic interventions by direct targeting of specific sites or cells.[12, 13] Individual cell targeting, however, remains a significant challenge in cancer nanomedicine and

has yet to be thoroughly demonstrated.[14] In the case of leukemia therapeutics, active targeting is required to allow specific delivery to leukemic cells in circulation and those in organ reservoirs such as bone marrow and spleen. It should be emphasized that targeting cannot be achieved at the expense of colloidal stability because the EPR effect cannot be relied upon and increased circulation half-life has been shown to increase delivery to bone marrow, spleen, and liver disease sites, where leukemia cells may frequently home.[15]

Given the unique challenge of nanoparticle-based delivery to leukemic cells, it is worthwhile to consider the optimal drug delivery platform. An effectively targeted nanocarrier for leukemia treatment would ideally possess the following combined characteristics: 1) uniform and controllable particle size and shape; 2) high colloidal stability under physiological and storage conditions; 3) minimal non-specific binding interactions, uptake by the MPS, or removal by excretory systems, allowing extended circulation time; 4) high specificity to diseased cells or tissues; 5) high capacity for and precise release of diverse therapeutic cargos; and 6) low cytotoxicity. Liposomes are one of the most successful classes of nanocarriers for achieving both passive and active targeted delivery, and numerous Food and Drug Administration (FDA) approved formulations exist.[16-19] Of candidate nanocarriers, liposomes exhibit many advantageous properties, including ease of synthesis, high biocompatibility, flexible formulation, targetability, and increased circulation times compared to free drugs.[7, 20-23] However, it has proven difficult to identify stable lipid formulations that allow drug encapsulation but prevent leakage.[24, 25] Polymeric based therapeutic nanocarriers have also been developed and several formulations are currently being tested in clinical trials.[18] Similar to liposomes, many polymer based nanocarriers are biocompatible and easy to manufacture, however they also suffer from limited stability *in vivo* and dose dependent toxicity.[26-28] Furthermore, both liposomes and

polymer based nanoparticles suffer the issues of invariant size and shape, uncontrollable, often burst release profiles, and highly interdependent properties, whereby changing one property, such as loading efficiency, affect numerous other properties, such as size, charge, and stability.[7, 20, 22, 23] By comparison, mesoporous silica nanoparticles (MSN) have controlled size and shape and are composed of high surface area (500 to > 1000 m^2/g) networks of uniformly sized pores whose size and surface chemistry can be varied widely to accommodate high payloads of disparate cargos.[29, 30] Furthermore, colloidal mesoporous silica is biodegradable and generally recognized as safe (GRAS) by the FDA.[31] The drawbacks of MSN are that often coatings are required to contain the cargo and shield surface silanols (≡Si-OH) and deprotonated silanols ($\equiv Si\text{-}O^-$) that are highly lipophilic and known to promote non-specific binding and MPS uptake.[32-34] In this context, MSN-supported lipid bilayers (protocells), a rapidly emerging class of nanocarriers, have unique attributes (**Scheme 1**). Protocells are formed by the encapsulation of the MSN core within a supported lipid bilayer (SLB) followed optionally by conjugation of polymers, such as PEG, and targeting and/or trafficking ligands to the surface of the SLB.[35-49] Protocells synergistically combine the advantages of liposomes, *viz.* low inherent toxicity and immunogenicity, and long circulation times, with the advantages of MSNs, *viz.* size and shape control and an enormous capacity for multiple cargos and disparate cargo combinations. Moreover, many studies have revealed that protocells and related MSN supported bilayer nanocarriers are stable at neutral pH but exhibit pH triggered cargo release under endosomal conditions.[36-42, 47]

To date, protocell based nanocarriers have shown to be effective for the delivery of multiple classes of cargos and cargo combinations to various cell types. [31] The majority of studies conducted have reported efficacy *in vitro*,[36, 37, 42] but numerous recent reports also show excellent

in vivo results, where passive and active targeting to solid tumors *via* the EPR effect have been demonstrated.[39-41, 43] However, the targeting of individual cells *in vivo* or in living systems has yet to be reported, and there have been no direct observations/determinations of *in vivo* colloidal stability. Here, based on our hypothesis that *in vivo* colloidal stability is paramount to achieving effective targeting, we explore how synthetic factors (*e.g.*, the lipid/silica ratio and ionic strength during SLB formation) and variation of modular protocell components (*i.e.*, MSN size, shape, and pore size, lipid bilayer fluidity, extent of PEGylation, and surface display of targeting ligands) influence colloidal stability as judged *in vitro* and *in vivo* by particle size stability and polydispersity and by direct observation *ex ovo* in a chick chorioallantoic membrane (CAM) model. We establish processing conditions whereby we achieve particle size monodispersity and size stability for protocells with differing size, shape, and pore morphology. Using optimized processing conditions, we further demonstrate long circulation times, avoidance of non-specific binding and minimal opsonization *ex ovo* and *in vivo*. Having achieved *in vivo* colloidal stability, we finally demonstrate targeted binding and cargo delivery to individual leukemia cells *in vitro* and *ex ovo* by direct observation in the CAM model.

RESULTS AND DISCUSSION

Synthesis Criteria for Monosized Protocells

Protocells were formed by fusion of zwitterionic lipid-based vesicles on monosized MSN (mMSN) cores synthesized with varying size, shape, and pore morphologies (See Experimental Section for detailed synthesis procedures). Vesicle fusion on silica glass substrates to form planar supported lipid bilayers has been extensively studied using atomic force microscopy, quartz crystal microbalance, deuterium nuclear magnetic resonance, surface plasmon resonance,

fluorescence microscopy and ellipsometry,[50-55] where the fusion process has been shown to involve vesicle adsorption followed (in some cases at a critical surface coverage) by vesicle rupture and desorption of excess lipid to form a bilayer separated from the glass surface by an intervening 1-2 nm thick water layer. Generally, the process of phospholipid vesicle fusion with smooth glass supports is governed by the same Derjaguin-Landau-Verwey-Overbeek (DLVO) forces that are responsible for colloid aggregation; hence, both vesicle-substrate and vesicle-vesicle interactions need to be considered. DLVO theory models the forces in such systems as consisting of an electrostatic interaction combining with a van der Waals attraction; as such, SLB fusion depends on pH, which controls the extent of deprotonation of surface silanol groups to form anionic ≡Si-O^- species above pH 2, and the ionic strength and cationic component of the buffer, which dictate, respectively, the Debye length (mediating electrostatic interactions) and the cation hydration diameter.[56] Cremer and Boxer studied fusion of positively charged, neutral and negatively charged vesicles onto glass as a function of pH (3-12) and ionic strength (0-90 mM). They found neutral and positively charged vesicles fuse under all conditions, whereas negatively charged vesicles fuse only above a critical ionic strength, which increased with pH (negative charge of silica surface). This is in keeping with expectations of DLVO theory as increasing ionic strength reduces electrostatic repulsion between vesicles and the glass surface.[56]

Although considerably fewer studies have been performed on vesicle fusion on silica nanoparticles, we anticipate that the mechanism and governing forces would be comparable but further influenced by the nanoparticle curvature. Using differential scanning calorimetry (DSC) in combination with dynamic light scattering (DLS), Savarala *et al*. studied the fusion of the zwitterionic 1,2-dimyristoyl-sn-glycero-3-phosphocholine (DMPC) vesicles on silica beads with diameters ranging from 100 to 4-6 nm at neutral pH and ionic strengths ranging from 0 to 0.75

mM NaCl. For a critical limiting ratio of lipid surface area to silica surface area of 1 (SA_{lipid}:SA_{silica} = 1), they found no (or very slow) vesicle fusion to occur in pure water and that higher ionic strengths were required to achieve fusion on successively smaller particles (100-20 nm).[57] 4-6 nm silica beads did not form supported lipid bilayers; rather, these beads appeared to associate with the exterior surfaces of the vesicles.[57] These results differ somewhat from flat surfaces and, in keeping with DLVO theory, suggest that, for progressively smaller particles, possible repulsive electrostatic interactions must be reduced by increasing ionic strength and/or attractive electrostatic interactions promoted by cation association with phosphocholine to compensate for increased membrane curvature (assuming conformal SLBs). This result is consistent with a study by Garcia-Manyes *et al*. that showed the surface charge of zwitterionic DMPC liposomes at neutral pH is negative at < 100 mM NaCl solution and positive at higher ionic strength. Excess lipid *i.e.,* SA_{lipid}:SA_{silica} > 1 appears to promote SLB formation on silica nanoparticles.[58] Mornet *et al.* studied the fusion of 30-50 nm diameter negatively charged 1,2-dioleoyl-*sn*-glycero-3-phosphocholine (DOPC)/ 1,2-dioleoyl-sn-glycero-3-phospho-L-serine (DOPS) vesicles on ~ 110 nm diameter spherical silica colloids by direct cryogenic transmission electron microscopy (Cryo-TEM). For SA_{lipid}:SA_{silica} = 15 and a buffer ionic strength of 152 mM, they observed conformal ~ 5 nm thick SLBs to form by a process involving conformal vesicle adsorption followed by rupture to form SLB patches.[59] Multiple adsorption and fusion events resulted in complete SLBs that conformed to the moderate surface roughness/microporosity of the Stöber silica nanoparticle surface.[59]

Numerous researchers have studied vesicle fusion on mesoporous silica macroparticles and nanoparticles as a means to form cell-like biomimetic materials[60] and lipid bilayer encapsulated nanoparticles for drug delivery.[36-43, 47] To date, nanoparticle studies have employed primarily

spherical cetyltrimethylammonium bromide (CTAB)-templated MSN formed by aerosol-assisted evaporation-induced self-assembly (EISA)[36, 37, 42, 48, 49, 61] or colloidal processing and characterized by worm-like or isotropic mesopores with diameters of about 2-3 nm.[38-41, 43, 47] Direct Cryo-TEM observations of protocells have shown the bilayer thickness to range from ~ 4-7 nm,[39, 42, 49, 61] corresponding to that measured for solid silica nanoparticle SLBs[59] or planar SLBs.[54] SLBs span the surface mesopores and remain conformal to the MSN surface, as we. and others, have shown by Cryo-TEM imaging (see, for example, **Figure 1)**. With respect to SLB formation, surface porosity decreases the areal fraction of silica at the nanoparticle surface and, assuming spanning lipid bilayers, reduces accordingly the possible magnitude of both van der Waals and electrostatic interactions that drive vesicle fusion. The fact that the modular MSN features of size, shape, pore size, pore volume, and pore morphology are important for their ultimate use as nanocarriers prompts us to ask how MSN physicochemical characteristics along with processing conditions influence vesicle fusion to form MSN-supported lipid bilayers aka 'protocells' for use as nanocarriers - where key criteria are size monodispersity, preservation of shape, and stability within physiologically relevant complex biological media.

To address this question we first chose to study monosized ~107 nm (hydrodynamic diameter measured by DLS) single-crystal-like mMSN composed of close-packed cylindrical pores confined within a hexagonally shaped nanoparticle that is disc-shaped in cross-section (**Scheme 1 and Figure 1A**). This highly asymmetric mMSN (referred to as Hexagonal mMSN) has opposing porous surfaces adjoined by grooved silica facets, thereby providing two distinct surfaces for vesicle fusion. To understand the roles of SA_{lipid}:SA_{silica} and ionic strength on vesicle fusion, we assembled protocells by mixing Hexagonal mMSNs with ~90 nm hydrodynamic diameter liposomes (composition = 1,2-distearoyl-*sn*-glycero-3-phosphocholine (DSPC),

cholesterol (-chol), and 1,2-distearoyl-*sn*-glycero-3-phosphoethanolamine-N-[methoxy(polyethylene glycol)-2000] (DSPE-PEG_{2000}) – where the molar ratio of DSPC:chol: DSPE-PEG_{2000} equaled 54:44:2 – **Table S1**). Liposomes were prepared by extrusion in a series of solutions consisting of 0 mM, 40 mM, 80 mM, 120 mM, 160 mM, and 320 mM ionic strength phosphate buffered saline (PBS). To complete the assembly process, the protocells were washed twice by centrifugation and resuspended in the final buffer solution with bath sonication and pipetting. Through variation of the lipid:silica ratio (wt:wt) and PBS concentration, we were able to adjust the SA_{lipid}:SA_{silica} from 0 (mMSN alone used as a control) to 4.22:1 and the ionic strength of the fusion conditions from 0 (water) to 160 mM spanning physiologically relevant ranges needed for *in vivo* applications (*vide infra*). We used a shape applicable model to calculate the external SA_{silica} from dimensional measurements of mMSNs obtained from TEM images (**Table S2**), using the pore volume obtained from nitrogen sorption data (**Table S2 and Figure S1**), and assuming 2.0 g/cm^3 as the silica framework density;[34] SA_{lipid} was calculated assuming 0.59 nm^2 as the phospholipid head group area;[62] and that cholesterol does not contribute to SA_{lipid} (**See calculation details in Supporting Information**). Using a Malvern Zetasizer Nano ZS, we measured the hydrodynamic diameter, polydispersity index (PdI), and zeta-potential (ζ) of protocells. **Figure 2A** plots hydrodynamic diameter and PdI as a function of SA_{lipid}:SA_{silica} and ionic strength. Consistent with our expectations from DLVO theory, without lipid, mMSNs (ζ = -28.1 mV, **Table 1**) aggregate with increasing ionic strength due to the reduced Debye length and concomitant reduction in the range of electrostatic repulsion. For samples prepared with SA_{lipid}:SA_{silica} < 1, the critical ratio needed to exactly cover the external surface of the mMSN with a single phospholipid bilayer, we observed severe aggregation that increases with ionic strength indicative of aggregation of exposed silica surfaces accompanied by

liposome adsorption and possible bridging. For samples prepared with SA_{lipid}:SA_{silica} > 1, we observed much more uniformly sized particles (PdI < 0.1) with hydrodynamic diameters *ca* 30 nm larger than the parent mMSN and zeta-potentials in the range (ζ = -3.3 mV, **Table 1**) consistent with the formation of a PEGylated zwitterionic SLB that shields the mMSN charge and provides a repulsive hydration barrier that stabilizes the protocells within biologically relevant media (*vide infra*). The exception are samples prepared in pure water (ionic strength = 0 mM) where for all SA_{lipid}:SA_{silica} we observed diameters 50 to 60 nm greater than the parent mMSN along with a trend of increasing PdI (**Table S3**). Samples prepared in pure water have a zeta potential comparable to the parent mMSN (ζ = -41.0 mV) and aggregate when transferred to 160 mM PBS (ζ = -28.1 mV). These ionic strength effects indicate fusion to be inhibited in pure water and are consistent with those obtained by Savarala *et al*. for fusion of single component 1,2-dipalmitoyl-sn-glycero-3-phosphocholine (DPPC) zwitterionic vesicles on solid 100 nm silica beads at SA_{lipid}:SA_{silica} = 1, where ionic strengths ≥ 0.05mM NaCl were needed for fusion as assessed by DSC.[57] Direct Cryo-TEM observation of Hexagonal mMSNs fused with DSPC-based liposomes at SA_{lipid}:SA_{silica} = 2.11:1 and ionic strength 40 mM show a conformal SLB with thickness 4.7 ± 0.5 nm (**Scheme 1 and Figure S2**) observed both on the porous and grooved surfaces (**Figure 1B**). We note the increased diameter of ~10 nm determined by TEM is inconsistent with the ~25 nm increase measured by DLS. Such discrepancies are often reported in the literature.[39, 63] Considering that the SA_{lipid} of a 90 nm liposome is less than that of a Hexagonal mMSN, multiple liposome fusion events are required to create a complete SLB (**Scheme 1**). In time-dependent Cryo-TEM, Mornet *et al.* showed liposome fusion on 100 nm colloidal silica nanoparticles to occur by a 'two-step' process involving adsorption followed by deformation and rupture.[59] Although we did not conduct a time-dependent Cryo-TEM study, we

did observe similarly evidence of deformed vesicles that conform to the mMSNs, which likely subsequently rupture to form SLBs in a similar 'two-step' process. We should note that, although it has been suggested that SLB formation on spherical, isotropic MSNs *via* probe sonication of dried lipid films in saline solution may proceed through a pathway other than vesicle fusion, implementing the identical probe sonication technique[39, 43] for Hexagonal mMSNs results in protocells indistinguishable (*i.e.*, nearly identical hydrodynamic diameter and PdI) from those formed by fusion with DSPC-based liposomes at SA_{lipid}:SA_{silica} = 4.22:1 and ionic strength 40 mM (**Table S4**). Finally, to help avoid any accompanying aggregation from occurring at the ionic strengths needed for vesicle fusion (and ultimately for *ex ovo* and *in vivo* applications, *vide infra*), we propose that conditions of excess of lipid and a low but sufficient ionic strength serve to increase the relative rate of vesicle fusion with respect to aggregation thus allowing the formation of monosized protocells with a low PdI (**Figure 2A**).

Our results on vesicle fusion on Hexagonal mMSN established a wide processing window in which to synthesize rather monosized protocells. As noted above, a SA_{lipid}:SA_{silica} ≈ 2:1 and ionic strength 40 mM appeared to represent an optimal fusion condition resulting in the smallest combination of hydrodynamic diameter and PdI (**highlighted by a green arrow in Figure 2A**). To test how this condition depended on bilayer fluidity or charge, we prepared vesicles containing unsaturated or saturated phosphatidylcholine (*e.g.,* DOPC or DSPC) or the cationic lipid 1,2-dioleoyl-3-trimethylammonium-propane (DOTAP) based on liposomal formulations reported in the literature (**Table S5**). We found, in general, that these conditions resulted in monosized protocells for zwitterionic lipid based formulations, whereas DOTAP resulted in aggregate formation. To further understand the influence of MSN physicochemical properties on protocell formation, we tested the optimized fusion conditions on a 'library' of MSNs with

differing shapes (*i.e.*, spherical or rod-like), particle size distributions (mMSN or EISA MSN), pore diameters (2.8 to 18 nm), and pore morphologies (aligned cylindrical, isotropic worm-like, and dendritic).[64-71] (See **Figure 1** and **Table S2** for a summary of the mMSN and EISA MSN physicochemical properties). As observed by direct Cryo-TEM observation, ~ 4 to 5 nm thick conformal SLBs formed on all of the tested particles (**Figures 1A-L and Figure S2**), and DLS showed a consistent increase in diameter of ~25 to 40 nm (**Figure 1M**). By visual examination, we observed a well-suspended and transparent dispersion of protocells in PBS contrasted with bare mMSNs that settle under normal gravity (**Figure 2B**). The exception was for spherical mMSNs prepared with dendritic pore diameters of ~18 nm. In this case we observed, by Cryo-TEM, vesicle adsorption and deformation on the mMSN surface but little evidence of complete SLB fusion (**Figure 3**). We propose that for this highly porous particle the magnitude of possible van der Waals and electrostatic interactions (that all scale nominally with surface silica concentration) is insufficient to cause rupture/fusion to form an SLB. Moreover, the topography of the silica surface is influential in the spreading process of the SLB, where 10 – 30 nm deep scratches were found to arrest spreading of egg phosphatidylcholine bilayers on borosilicate glass due to unfavorable bending interactions needed to maintain conformity.[56, 72] It is likely that for mMSNs there is a critical pore size above which the highly contoured regions of the pore arrest spreading and fusion. This pore size should be sensitive to the SLB composition, which dictates the bending modulus. Using unsaturated lipids and, potentially, decreasing the cholesterol content might be expected to make the membrane more flexible and promote SLB formation on mMSNs with larger pore size,[73, 74] however, at the cholesterol concentration (44%) used in our experiments, it is unlikely that the transition temperature (T_m) of the phosphatidylcholine SLB component is a major factor in size stability.[75] It is also conceivable

that fusion might be promoted by doping the buffer with divalent ions like Ca^{2+} or Mg^{2+} that, through several possible electrostatically mediated pathways, are known to promote vesicle fusion on glass.[76, 77] Finally adsorption of drugs within the pores would in essence increase the solid fraction of the surface and potentially promote attractive DLVO interactions and vesicle fusion.

Factors Influencing Colloidal Stability of Monosized Protocells for Use *in vivo*

Having established a generalized process by which to reliably form monosized protocells *in vitro*, we next studied how the physicochemical properties of the SLB influence colloidal stability in complex biological media. As noted above, *in vivo* colloidal stability is crucial to the realization of both passive and active targeting as any process that non-selectively removes nanoparticles from circulation reduces concomitantly the number of particles that could accumulate in the tumor microenvironment due to the EPR effect or those that are available to selectively bind to target cells or tissues. Despite its importance, few papers unambiguously establish the stability of nanocarriers, which may in part explain inconsistent and unreproducible results in the literature, which are now generally recognized.[78-80] Problematic is that *in vivo* colloidal stability is difficult to predict from *in vitro* measurements. For example, we recently showed cationic MSNs with identical size, shape, and surface charge (and therefore indistinguishable according to NCI NCL standards)[78] to have completely different circulation and non-specific binding behaviors as elucidated by direct observation *ex ovo* in a CAM model[81] and SPECT imaging in a rat model (Adolphi *et.al.* private communication). Here, we evaluated colloidal stability by determination of hydrodynamic size and polydispersity index in complex biological media and by direct observation in the CAM model.

First, we examined how the encapsulating SLB and its fluidity affected long term stability compared to the bare mMSN surface. We prepared liposomes with zwitterionic lipids using either unsaturated DOPC or saturated DSPC as the major liposome component. Our comparison between DOPC and DSPC is ideal because these lipids possess nearly identical molar mass, have the same acyl tail length, and yet exhibit T_m (-20°C and 55°C respectively) below and above the storage and physiological temperatures (22°C and 37°C, respectively). Additionally, the *cis*-configuration double bonds present in the DOPC acyl chains (absent in DSPC) are highly susceptible to oxidation, which can lead to structural instability.[82] We prepared unsaturated DOPC-based (composition = DOPC, chol, and 1,2-dioleoyl-*sn*-glycero-3-phosphoethanolamine-N-[methoxy(polyethylene glycol)-2000] (DOPE-PEG_{2000}) – DOPC:chol:DOPE-PEG_{2000} mol ratio of 54:44:2) and saturated DSPC-based (composition = DSPC:chol:DSPE-PEG_{2000} mol ratio of 54:44:2) vesicles by extrusion as previously described. Liposome compositions and hydrodynamic diameters are summarized in **Table S1**, where all possessed a hydrodynamic diameter < 100 nm and low PdI value < 0.2. Liposome to mMSN fusion was achieved in 40 mM PBS as described earlier; then protocells were finally redispersed in 160 mM PBS. The formation of a complete SLB surrounding the MSN cores was verified by combined techniques: DLS measurements showed the hydrodynamic diameter to increase uniformly by ~ 30 nm compared to mMSNs, while maintaining a low PdI (< 0.1) (**Tables 1 and S2**). Zeta-potential measurements indicated the Hexagonal mMSN protocells to have a zeta potential (-3.3 mV) similar to the corresponding zwitterionic liposomes (-2.9 mV) and much lower than the mMSN (-28.1 mV) (**Table 1**). Direct observation by Cryo-TEM (**Figure 1B**) showed the presence of a uniform conformal SLB surrounding the mMSN cores.

Figure 4A shows changes in hydrodynamic size of protocells for 72 h at 37°C compared to bare mMSN controls (see **Table S6** for corresponding PdI). Whereas the hydrodynamic size of bare mMSNs increases within minutes of transfer to PBS at room temperature, and more rapidly at 37°C, both DOPC-based and DSPC-based protocells maintain uniform size for 24 h. Our results suggest that the colloidal stability of the protocells is due primarily to the zwitterionic SLB component rather than the PEG component, as the trends observed for DOPC and DSPC-based protocells prepared with and without PEG are nearly identical (**Figure 4A**). The stabilizing effect of the zwitterionic SLB can be attributed to several factors. Zwitterionic coatings are shown to increase nanoparticle stability in high salt concentration solutions due to hydration repulsion which also minimizes non-specific protein adsorption in serum containing solutions.[83-86] In addition, the presence of both positively and negatively charged functional groups on nanoparticle surfaces has been shown to increase solubility in water over a wide pH range, limit non-specific interactions with cultured cells, and display a non-toxic profile upon interaction with cells, based on cell viability assessment.[87] That the protocells are encapsulated completely within a zwitterionic SLB is evidenced by the hydrodynamic size / PdI change of bare mMSNs, increasing from 106.9 nm / 0.050 to 193.4 nm / 0.292 in PBS after centrifugation (**Table 1**) along with their rapidly settling in PBS solution (**Figure 2B**); incomplete SLB coverage would similarly result in the formation of irreversible aggregates *via* electrostatic destabilization and van der Waals forces, *vide supra*.

Concerning the influence of lipid bilayer composition on long-term stability, we find that, although both DOPC-based and DSPC-based protocells are stable for 24 h, the size of both PEGylated and non-PEGylated DOPC-based protocells increases progressively from 24 to 72 h in PBS. In comparison, DSPC-based protocells remain stable for > 72 h at 37°C in PBS (**Figure**

4A) and for over 6 months at room temperature (**Table S7**). To assess the possible role of lipid oxidation as being the cause of the instability of DOPC-based protocells, we prepared protocells in de-oxygenated PBS and determined their hydrodynamic size during storage for 7 days at 37°C. Interestingly, we find DOPC-based protocells to remain stable in an oxygen reduced buffer, whereas they aggregate in standard PBS. In comparison, the presence or absence of oxygen made no difference in DSPC-based protocell size stability (**Figure S3**). This result indicates that the double bonds present in the acyl chains of unsaturated lipids are susceptible to oxidation and that lipid oxidation plays a significant role in the long-term stability of the corresponding protocells, where lipid oxidation presumably compromises the SLB leading to aggregation. Storage of protocells prepared with unsaturated lipids in de-oxygenated solvents should significantly increase 'shelf-life' needed for practical clinical translation.

Although, we have noted that colloidal stability of the protocells is primarily due to the zwitterionic SLB component, modification of nanocarriers with hydrophilic polymers has been widely shown to prolong *in vivo* circulations times, reduce protein adsorption, and reduce phagocytosis by immune cells.[88] Therefore, we used only PEGylated protocells to examine the influence of T_m in a more complex medium. We prepared protocells in PBS and then transferred them to a cell culture medium containing fetal bovine serum. Similar to the previous experiment, DSPC-based protocells maintain size stability for > 72 h at 37°C (**Figure 4B**), indicating minimal protein binding and destabilization of the SLB. Interestingly, we observe the identical size stability for DOPC-based protocells in complete media, suggesting that protein adsorption stabilizes the DOPC-based SLB and/or provides a steric barrier toward fusion and aggregation despite there being no measureable increase in hydrodynamic diameter.

Overall, we find that the zwitterionic SLB confers excellent colloidal stability to the protocell in physiologically relevant media. Both unsaturated and saturated SLBs prepared with and without PEG have greatly enhanced stability compared to the parent mMSN. Nevertheless, the measured long-term stability of DSPC-based monosized protocells, compatibility with the majority of mMSN cores tested, and potential to incorporate functional modifications to PEGylated lipids, in particular amine terminated 1,2-distearoyl-*sn*-glycero-3-phosphoethanolamine-N-[amino(polyethylene glycol)-2000] (DSPE-PEG_{2000}-NH_2) which can be chemically modified with a functional component, prompted us to choose the DSPC-PEG-based protocell formulation for further *in vitro, ex ovo,* and *in vivo* studies.

Influence of Protocell Size Dispersity on *in vitro* and *ex ovo* Performance

For the development of therapeutic nanocarriers specifically targeted to leukemia cells, prolonged circulation times are needed to enhance the probability of delivery to distributed cells within the blood, marrow, and other tissue spaces, and, it is reported that particle size is an important determinant in delivery to tissue sites characteristic of this disseminated disease.[15] Therefore, it is of interest to understand the effect of protocell size dispersity on *in vivo* performance. Potentially, a broad particle size distribution could effect or direct broad dissemination of protocells to differing body tissues in addition to the peripheral vasculature and other tissues (liver, spleen, bone marrow) which may harbor leukemic cells, or, protected tissues which serve as sanctuaries for leukemic cells (testes, brain) and are frequent sites of recurrent or relapsed disease following systemic chemotherapy treatment. However it is presently unclear as to how particle size polydispersity influences particle entrapment, non-specific binding, and circulation time. In order to assess the dependence of polydispersity on non-specific binding and circulation, we compared monosized protocells with protocells assembled from MSN cores

prepared by aerosol assisted EISA as previously reported.[89] EISA cores are characterized by spherical MSNs with a power law particle size distribution ranging from ~20 to ~800 nm (see TEM images in **Figures 1K, 1L, and S4**) that results from the aerosol droplet size distribution of the aerosol generator. EISA MSNs have a pore diameter of ~ 2.5 nm and a zeta-potential of ~ -31 mV,[48] comparable to those of Hexagonal mMSNs, so the comparison of their behaviors depends principally on polydispersity (See **Table S2** for other physicochemical parameters of the EISA MSN and protocells). Hexagonal and EISA protocells were prepared by fusion of vesicles with composition, DSPC:chol:DSPE-PEG_{2000} mol ratio of 54:44:2 according to methods described previously. The hydrodynamic diameter and PdI of EISA protocells was ~715 nm and 0.434 compared to ~ 137 nm and 0.085 for hexagonal protocells (**Figure 1M and Table S2**).

To investigate the role of polydispersity on *in vitro* MSN and protocell non-specific binding interactions, we incubated human endothelial cells (EA.hy926) with either fluorescently labelled EISA or mMSN cores and their corresponding protocells (20 μg/mL) for 4 h with complete medium under normal cell culturing conditions. Flow cytometry analysis showed both EISA and mMSN particles to have significant levels of non-specific binding to EA.hy926 cells (**Figure S5**) where for EISA MSN the extended breadth of the FL2-H intensity curve reflected the size (and therefore) fluorescence intensity distribution of individual MSNs. Correspondingly, the fluorescence intensity binding curve for mMSNs was rather monodisperse. For both EISA and mMSN derived protocells, we observe a 20-fold decrease in non-specific binding relative to the parent core particle (**Figure S5, see also fluorescence microscopy images in Figure S6**). This indicates that the conformal and complete SLB serves to effectively shield lipophilic surface silanol groups (≡Si-OH) and anionic deprotonated silanols (≡Si-O^-) present on the bare MSN and known to promote internalization *via* micropinocytosis and other non-specific endocytotic

pathways.[33] Our findings underscore the importance of the SLB in helping to prevent non-specific cell binding events, and support previous reports demonstrating minimal nonspecific cell binding affinity of polydisperse EISA protocells *in vitro*.[36, 42]

However, as previously noted, *in vitro* studies of nanoparticle behavior may be poor indicators of *in vivo* outcomes as they lack the complexities of *in vivo* conditions which present major obstacles to nanoparticle stability and target cell binding.[90] These obstacles include flow dynamics within the diverging and converging vasculature, opsonization by plasma proteins, uptake by the mononuclear phagocyte system, and the need for translocation across the capillary bed for tissue penetration. To assess MSN and protocell behavior in a more relevant model, we employed the CAM model as an *in vivo (ex ovo)* model of the vascular system in which to observe nanoparticle circulation, flow characteristics, non-specific interactions, and particle stability in a living system using intravital imaging.[81, 91, 92] Fluorescently labeled nanoparticles can be injected intravenously into the CAM vasculature and imaged over time. As investigated previously *in vitro*, we examined mMSN cores as well as EISA and mMSN protocells to assess the influence of the SLB and polydispersity on biodistribution in this more complex *ex ovo* CAM environment. The influence of the SLB on nanoparticle flow dynamics and non-specific binding was immediately evident as bare mMSN cores bound to endothelial cells and arrested in the vessels of the CAM within 5 minutes of injection (**Figure S7A**) and were largely taken up by phagocytic white blood cells after 30 minutes, reducing correspondingly the concentration of circulating mMSNs (**Figure S7B**). By comparison, monosized protocells exhibited significantly lower non-specific binding and uptake by white blood cells leading to greatly improved circulation characteristics (**Figures 5A and 5B**). (A representative video of stable monosized protocell circulation is provided in Supporting Information (**Video S1**).) Striking was the

contrast between mMSN and EISA protocells. Even though the *in vitro* outcomes were nearly identical, rapid sequestration of EISA protocells by immune cells, aggregation, and diminished circulation was noted within 5 minutes in the vascular CAM system (**Figure 5C**), with a more pronounced effect after 30 minutes (**Figure 5D**). The rapid uptake and reduced circulation are likely due to polydispersity leading to the majority of particles falling within a size range that either encourages immune cell uptake or advances unpredictable systemic circulation and distribution.[93] The CAM results highlight the need for reduced size polydispersity to maintain circulation within highly vascularized networks and elucidate a major limitation of *in vitro* models in predicting *in vivo* results. In this regard, we view the vascularized CAM model to improve greatly on *in vitro* models of specific and non-specific binding and more realistically assess the behavior of nanoparticles designed for *in vivo* use.[81]

Biocompatibility and Protocell Size Stability *ex ovo* and *in vivo*

Previous studies have shown mesoporous silica to be a biocompatible material; however, the interpretation of the overall biocompatibility of MSN-based nanocarriers is complex due to several factors including methods of synthesis, physicochemical properties, size distribution, and surface modifications.[94] Therefore, to assess the influence of the SLB on biocompatibility and to determine the uniformity of the SLB coating, we incubated mMSNs and protocells with human red blood cells (hRBCs). We observed that the hemolytic activity and potential toxicity of bare mMSNs can be completely abolished with a SLB (**Figure S8**). This result supports evidence of a complete (defect-free) lipid bilayer coating that screens silanols (≡Si-OH) and anionic deprotonated silanols (≡Si-O^-) implicated in hemolysis[32] and, thereby, provides enhanced biocompatibility of the protocells vis-à-vis mMSNs.

Earlier we established that monosized protocells maintain long-term colloidal stability in PBS and complete cell culture media; however, we sought a more rigorous test for our platform under more dynamic conditions. Protein corona formation onto nanoparticle surfaces has been shown to occur immediately upon exposure to a live animal system.[95] Thus, we examined protocell size stability after intravenous injection and circulation because, to the best of our knowledge, no current reports have examined nanoparticle stability post-injection. Fluorescent nanoparticle labeling provided useful qualitative analysis of stability within the CAM vasculature, which led us to seek quantitative measures of protocell size after separation from blood samples extracted post-injection from both CAM and *in vivo* mouse models. We detected fluorescent protocells in whole blood samples extracted from the CAM (**Figure 6A**); we then separated protocells from whole blood by centrifugation and the measured hydrodynamic size. Remarkably, the average protocell size is nearly identical pre- and post-injection (**Figure 6B**). In addition, we examined protocell size after circulation for multiple time points and found only a modest, time-dependent, average hydrodynamic diameter increase of 9% at 30 minutes and increasing to 23% at 240 minutes (**Figure S9**). We further validated *in vivo* stability characteristics by intravenous tail vein injection of protocells into a BALB/c mouse. After 10 minutes of protocell circulation, we extracted blood from the mouse, imaged fluorescent protocells in whole blood (**Figure 6C**), separated protocells using centrifugation, and found protocells maintain size stability in a mouse model (**Figure 6D**). Thus, we demonstrated qualitative and quantitative confirmation of both *ex ovo* and *in vivo* protocell stability in unique and separate model systems. While these data indicate that the protocell platform possesses a distinctive ability to circulate and avoid aggregation in a complex living system for a short period of time, we acknowledge the need for a more comprehensive analysis of protocell circulation and biodistribution in relevant *in vivo*

animal models of disease in order to provide a more complete pre-clinical understanding of *in vivo* protocell performance.

Protocell Targeting Specificity *in vitro* and *ex ovo*

Once we verified the biological compatibility and *in vivo* stability of the monosized protocell platform, we examined receptor specific targeting both *in vitro* and *ex ovo*. As a model system we chose a human B cell precursor acute lymphoblastic leukemia (ALL) cell line (REH) that was engineered to express the epidermal growth factor receptor (EGFR) and we compared the performance of these REH-EGFR leukemia cells to the parental (EGFR-negative) cell line so as to have a matched negative control for our experiments. Targeting was accomplished using the NeutrAvidin/biotin conjugation strategy to modify an amine functionalized SLB (prepared with mol ratio DSPC:chol:DSPE-PEG_{2000}-NH_2 = 49:49:2 – **Table S1**) with anti-EGFR monoclonal antibodies as depicted in **Scheme 1**.

To examine targeting specificity, we compared protocell interactions with both the human REH parental cell line controls and also with , a murine B precursor ALL cell line (Ba/F3) also lacking EGFR. We compared the performance of these parental EGFR-negative control cell lines to corresponding REH and Ba/F3 clones engineered to express ectopic human EGFR, designated REH-EGFR and Ba/F3-EGFR, respectively.[96] To assess the kinetics of protocell binding, we incubated anti-EGFR antibody-labeled fluorescent protocells with REH parental and REH-EGFR cells for various time points *in vitro*. We observed significant binding within 5 minutes and maximal binding at 30 minutes of incubation in complete media under normal cell culture conditions by both flow cytometry (**Figure 7A**) and fluorescence microscopy (**Figure S10**). As expected, from the absence of non-specific binding shown previously (**Figures S5 and S6**), protocell binding was not observed in the REH parental cell line (**Figure 7B**), nor did we

observe non-targeted (anti-EGFR negative) protocell binding to either REH or REH-EGFR cell lines, as measured by flow cytometry (**Figure S11**). To confirm that target specific binding is not cell line specific, we incubated anti-EGFR protocells with Ba/F3 and Ba/F3-EGFR cells for 60 minutes using previously described conditions for REH and REH-EGFR cells. Using fluorescence microscopy, we observed minimal non-specific binding of EGFR-targeted protocells to parental Ba/F3 cells; conversely we observed significant selective binding to Ba/F3-EGFR cells (**Figures S12A and S12B**). Flow cytometry analyses revealed the targeted protocells had a much greater binding affinity to Ba/F3-EGFR cells compared to the control Ba/F3 parental cell line *in vitro* (**Figures S12C and S12D**).

To provide an *in vivo* relevant assessment of targeted binding, we evaluated the characteristics of the targeted protocell binding using real-time intravital imaging in the *ex ovo* CAM model of the vasculature. We injected green fluorescent labelled REH or REH+EFGR cells into the CAM and allowed the cells to arrest in the capillary bed (~ 30 minutes). Next, we injected either anti-EGFR targeted or non-targeted red fluorescent protocells into the CAM and imaged protocell flow and binding dynamics at 1, 4, and 9 h time points. We observed protocells flowing in the blood stream at 1 h (**Figure 8A**), as well as cell specific binding of the anti-EFGR protocells to the REH-EGFR cells. While flow had diminished at 4 and 9 h time points, we still observed targeted protocell co-localization with the target cells (**Figures 8B and 8C**). Since we observed a significant targeted protocell binding to REH-EGFR cells at 1 h and our *in vitro* experiments showed binding within 5 minutes, we sought to capture targeted protocell binding within a vascularized system in real time; thus, we performed intravital imaging in the CAM immediately after protocell injection and observed several binding events on multiple cells (**Figure 9 and Video S2**) within 5 to 10 minutes post protocell injection. To verify that protocell binding was

indeed EGFR specific, we tested anti-EGFR targeted protocells with REH cells and non-targeted protocells with REH and REH-EGFR cells lines and found similar flow patterns for the protocells at 1 h time points; however, the protocells did not interact with the leukemia cells (**Figure S13**) providing further support for our targeting methodology. As a final step, we investigated whether protocell binding was influenced by the particular engineered cell line. We injected Ba/F3-EGFR cells *ex ovo*, followed by anti-EGFR protocell injection, and observed target cell specific binding at 10 minutes and 20 h (**Figure S14**). Based on these findings, we are confident that we have engineered biologically stable protocells with a high degree of specificity evaluated both *in vitro* and by intravital imaging in the CAM model to bind to individual target cells.

Protocell Cargo Loading and Delivery to Targeted Cells

Next, we evaluated the cargo loading and targeted delivery characteristics of monosized protocells both *in vitro* and *ex ovo*. As a surrogate for a true drug, we chose YO-PRO®-1, a green fluorescent membrane impermeable molecular cargo. We added YO-PRO®-1 to red-fluorescent mMSNs, fused liposomes, and conjugated anti-EGFR targeting components to the surface following the steps illustrated in **Scheme 1**. Anti-EGFR targeted protocells loaded with YO-PRO®-1 exhibited similar size and zeta potential characteristics to unloaded protocells assembled under identical conditions (**Table S8**). We calculated a 25% loading efficiency by disrupting the SLB of loaded protocells with a detergent and measuring the fluorescence intensity of YO-PRO®-1 extracted in DMSO (**Details in the Experimental Section**). Next, we assayed targeted protocell internalization as a measure of time using an acid wash technique to remove surface bound protocells at specific time points. Using flow cytometry and fluorescence microscopy, we found that anti-EGFR targeted protocell binding and internalization occurs

within 1 h (**Figures 10A and S15**); however cargo release, as measured by intracellular green fluorescent cargo diffusion, occurred more slowly (**Figures 10B, and S15**).

To assess protocell targeted cell specific killing, *in vitro*, we chose gemcitabine (GEM) as a model anti-cancer cytotoxic agent due to its low molecular weight, which allows it to access and adsorb to the high surface area mMSN mesostructure, as well as its relative membrane impermeability,[97, 98] which allows the SLB to essentially seal the cargo in the protocells and to prevent off-target effects due to drug leakage. Moreover, GEM requires a nucleoside transporter to cross the cell membrane, and reduced expression of the nucleoside transporter is known to be associated with gemcitabine resistance.[97, 98] Furthermore, the plasma half-life of GEM is only 8-17 minutes due to rapid conversion to an inactive form that is excreted by the kidneys;[97] therefore, GEM requires frequent doses to overcome this clearance rate. Thus, encapsulation of GEM within a targeted protocell may overcome many of the challenges associated with conventional GEM-based therapy.

We assessed cargo delivery using REH and REH-EGFR cells incubated with GEM loaded anti-EGFR protocells *in vitro*. To prepare GEM loaded, anti-EGFR targeted protocells, we suspended mMSNs in a solution of GEM prepared in H_2O then assembled protocells by fusing GEM-soaked mMSNs with liposomes following the steps illustrated in **Scheme 1**. The supernatant from each step was collected and combined; the GEM content was determined by measuring the absorbance (265 nm) using a microplate reader. Our described GEM loading strategy resulted in a calculated 15 wt. % GEM encapsulation (**Details in Experimental Section**). We found cargo loading did not influence the final targeted protocell size (**Table S8**), a result consistent with GEM loading of the internal mesoporosity.

To examine the drug release profile under simulated lysosomal conditions, we prepared GEM loaded protocells in PBS, then dialyzed the samples in either PBS (pH 7.4) or 1M citrate buffer (pH 5.0) for 72 h at 37 °C. We measured the absorbance (265 nm) of supernatant collected at several time points to determine the quantity of GEM released under these conditions. We observed a greater total drug release percentage at pH 5.0 (~30%) compared to pH 7.4 (~14%) after 72 h (**Figure S16**). We also observed a significant hydrodynamic size increase at 48 h in pH 5.0, correlating with the increase in drug release observed at the same time point, while protocells maintain size stability at pH 7.4 under the same experimental conditions (**Figure S16**). These data suggest that drug release is increased at a lower pH primarily due to SLB destabilization as evidenced by aggregation. However, we are only examining the influence of a single variable (pH), while other conditions exist in the lysosomal pathway including degradative enzymes, for example phospholipase A2,[99] which could affect drug release. Therefore, we next examined the functional release of GEM as a measure of cell viability *in vitro*. To evaluate the target specific drug delivery, we incubated REH and REH-EGFR cells with increasing concentrations of anti-EGFR GEM-loaded protocells in complete media under normal culturing conditions. We observed a distinct EGFR-target specific decrease in viability correlating to an increase in targeted protocell concentration (**Figure 10C**). Finally, we assessed the killing specificity of free-GEM, and observed decreased cell viability with increasing GEM concentration in a non-specific manner (**Figure 10D**). To verify that the cargo is responsible for the killing as opposed to the protocell itself, we incubated anti-EGFR targeted protocells with REH and REH-EGFR cells with increasing concentrations and observed no loss in viability for up to 200 μg/mL of protocells (**Figure 10E**). Worth mentioning, a subset of REH-EGFR engineered cells appear to lose EGFR expression over time (**Figure 10F and Figure 7A – red**

arrow); therefore, the remaining viable cells in the maximum dose tested (50 μg protocells / 30 μM GEM) (**Figure 10C**) are likely to be EGFR negative.

To test targeted binding and cargo delivery in a complex living system, we injected the CAM with fluorescent labelled REH-EGFR cells followed after 30 minutes by injection of YO-PRO®-1 loaded anti-EFGR protocells. (Prior to intravital imaging a lectin vascular stain was injected to provide contrast in the blood vessels). Intravital fluorescent imaging of the steps of binding, internalization, and cargo release was performed at 4 and 16 h post *ex ovo* injection based on *in vitro* experiments (**Figure S15)** that showed binding in as little as five minutes **(Figure 7A)** but YO-PRO®-1 delivery and release to the cytosol to occur between 1 and 8 h **(Figure 9B)**. **Figure 11A** shows target specific binding to an individual REH+EFGR cell trapped within the CAM vasculature 4 h post injection. There is no evidence of cargo release. **Figure 11B** shows targeted binding to an individual REH+EFGR cell 16 h post injection, where YO-PRO®-1 is dispersed throughout the cell similar to the *in vitro* results (**Figure S15).** To better illustrate the targeted protocell binding, internalization, and cargo release at 16 h, we imaged 0.25 μm sections of a targeted cell and stacked the images into a video in the supporting information (**Video S3**).

We recognize the need to assess the targeted killing of REH-EGFR cells by anti-EGFR GEM-loaded protocells in an animal model; however, determining conclusively that protocells are directly responsible for killing target cells in the *ex ovo* system is difficult, since many of the cells are eliminated by the chick immune system and possess a limited life-span in this host. Further targeted delivery studies in a murine leukemia model to test protocell co-localization and disease elimination must be evaluated. Nonetheless, our demonstrated highly specific targeted drug delivery *in vitro* combined with surrogate drug delivery *ex ovo* provide compelling

evidence for the single-cell targeting utility of the monosized protocell therapeutic delivery platform.

CONCLUSIONS

Here, by systematically evaluating the influence of SA_{lipid}:SA_{silica} and ionic strength on vesicle fusion to MSNs, we established a robust processing protocol to prepare colloidally stable mMSN supported lipid bilayers aka protocells characterized by size uniformity (PdI < 0.1) and long-term stability in biologically relevant media. The protocol we developed (SA_{lipid}:SA_{silica} ≈ 2:1 and ionic strength = 40 mM) using prismatic Hexagonal mMSNs was shown to be transferable to MSNs of differing size, shape, and pore morphology. Only for mMSNs prepared with the largest pores (~ 18 nm) did we find fusion not to occur – presumably due to reduced van der Waals and electrostatic interactions and/or surface roughness arrested bilayer spreading.

Having established a robust process to prepare monosized protocells, we evaluated their long-term stability in biologically relevant media *in vitro* as well as in *ex ovo* and *in vivo* models and systems. We found that zwitterionic SLBs prepared with or without PEG conferred excellent stability to the protocells compared to the parent mMSN. DSPC-based SLBs were shown to have longer-term stability than DOPC-based protocells in PBS at 37°C. However, DOPC-based protocell stability was restored by the removal of soluble oxygen. Furthermore, protocells prepared with both unsaturated DOPC and saturated DSPC SLBs were stable for over 72 h in FBS enriched media suggesting that preparation and storage in de-oxygenated buffer or exposure to proteins prior to use would allow either formulation to be implemented *in vivo* depending on the desired characteristics of the specific application. While saturated SLBs, with demonstrated stability in standard PBS are easier to prepare and store, we believe protocells prepared with

unsaturated SLBs could be used for *in vivo* targeting, where the fluid bilayer could support lateral diffusion of targeting ligands, enabling high avidity binding with low targeting ligand density, as previously reported *in vitro*.[42]

The behavior of DSPC-PEG-based protocells was assessed *ex ovo* in the CAM model whose diverging and converging vasculature recapitulates features of the liver and spleen and whose immune system is replete with professional phagocytic cells including Kupffer cells and sinusoidal macrophages. High-speed intravital imaging of protocells and target cells injected into the vasculature of the CAM model allowed direct observation of circulation, non-specific binding to the endothelium, uptake by white blood cells, and binding to target cells in a complex setting, containing blood proteins and a developing immune system. While *in vitro* assessment is standard practice and provides important information, we contend it lacks the complexity to accurately forecast *in vivo* outcomes. For example, by comparing monosized protocells with highly size polydisperse protocells, we demonstrated size monodispersity to be important for avoiding arrest in the capillary bed and uptake by immune cells. Monosized DSPC-PEG-based protocells, shown to be stable within complex CAM and *in vivo* mouse models, were conjugated with anti-EGFR antibodies while maintaining size monodispersity.

Flow cytometry combined with fluorescence microscopy showed a high degree of binding specificity of EGFR-targeted protocells to REH-EGFR and Ba/F3-EGFR ALL cells compared to EGFR-negative parental control cells. Using intravital imaging in the CAM, we directly observed selective binding of EGFR-targeted protocells to individual leukemic cells followed by delivery of a membrane impermeant cargo, while avoiding non-specific binding to endothelial cells and uptake by immune cells. Overall, we demonstrate that zwitterionic monosized protocells prepared by vesicle fusion on mMSN cores have long-term stability in complex

biological media as judged by intravital imaging in the experimentally accessible CAM model. Colloidal stability is crucial to achieving targeting to individual (leukemic) distributed cells, where the EPR effect is inoperative.

Finally, we demonstrated the highly specific therapeutic efficacy of targeted protocells by delivery of the cytotoxic anti-cancer drug cargo gemcitabine to an engineered EGFR-expressing leukemic cell line, while sparing EGFR-negative parental cells from off-target effects. Further, we confirmed the biocompatibility of the protocell platform. We believe our optimized monosized protocell design has great potential for the *active* targeting, detection and treatment of highly disseminated metastatic cells including difficult to target circulating leukemia cells as well as combined *passive and active* tumor targeting employing the EPR effect. The logical next steps will include identifying the size limitations of the protocell platform, testing of alternative targeting conjugation chemistries, identifying unique targeting ligands for important diseases, and examining a large array of therapeutic cargo types to be evaluated *in vitro, ex ovo,* and ultimately in *in vivo* models of leukemia, including xenograft and primagraft model systems.

EXPERIMENTAL SECTION

Materials: All chemicals and reagents were used as received. Ammonium hydroxide (NH_4OH, 28-30%), 3-aminopropyltriethoxysilane (98%, APTES), ammonium nitrate (NH_4NO_3), benyldimethylhexadecylammonium chloride (BDHAC), n-cetyltrimethylammonium bromide (CTAB), N,N-dimethyl formamide (DMF), dimethyl sulfoxide (DMSO), rhodamine B isothiocynate (RITC), tetraethyl orthosilicate (TEOS), Triton X-100, and Buffer solution pH 5.0 (citrate buffer) were purchased from Sigma-Aldrich (St. Louis, MO). Hydrochloric acid (36.5-38%, HCl) was purchased from EMD Chemicals (Gibbstown, NJ). Absolute (99.5%) and 95%

ethanol were obtained from PHARMCO-AAPER (Brookfield, CT). 1,2-dioleoyl-sn-glycero-3-phosphocholine (DOPC), 1,2-distearoyl-snglycero-3-phosphocholine (DSPC), 1,2-dioleoyl-*sn*-glycero-3-phosphoethanolamine-N-[methoxy(polyethylene glycol)-2000] (ammonium salt) (DOPE-PEG_{2000}), 1,2-distearoyl-sn-glycero-3-phosphoethanolamine-N-[methoxy(polyethylene glycol)-2000] (ammonium salt) (DSPE-PEG_{2000}), 1,2-distearoyl-*sn*-glycero-3-phosphoethanolamine-N-[amino(polyethylene glycol)-2000] (DSPE-PEG_{2000}-NH_2) phospholipids and cholesterol (chol, ovine wool, >98%) were purchased from Avanti Polar Lipids (Birmingham, AL). Hoechst 33342, Traut's reagent, YO-PRO®-1, and maleimide-activated NeutrAvidin protein were obtained from Thermo Scientific (Rockford, IL). Alexa Fluor®488 phalloidin, CellTracker™ Blue CMAC dye, and CellTracker™ green CMFDA dye were purchased from Life Technologies (Eugene, OR). Heat inactivated fetal bovine serum (FBS), 10X phosphate buffered saline (PBS), 1X trypsin-EDTA solution, and penicillin streptomycin (PS) were purchased from Gibco (Logan, UT). Dulbecco's Modification of Eagle's Medium with 4.5 g/L glucose, L-glutamine and sodium pyruvate (DMEM) and RPMI-1640 medium were obtained from CORNING cellgro (Manassas, VA). Gemcitabine (GEM) was purchased from LC Laboratories (Woburn, MA). Anti-EGFR antibody [EGFR1] (Biotin) (ab24293) was purchased from Abcam (Cambridge, MA). CellTiter-Glo® 2.0 Assay was purchased from Promega (Madison, WI). DyLight 649 Lens Culinaris Agglutinin was purchased from Vector Laboratories (Burlingame, CA). Spectra-Por® Float-A-Lyzer® G2 Dialysis Device MWCO: 3.5 – 5 kD was purchased from Spectrum Laboratories Inc. (Rancho Dominguez, CA).

Synthesis of mMSNs composed of hexagonally arranged cylindrical pores (2.8 nm pore size), Hexagonal mMSN. To prepare monosized dye-labeled mMSNs (~95 nm in diameter, Figure S1, ~130 nm in hydrodynamic size in D.I. water), 3 mg of RITC was dissolved in 2 mL of DMF

followed by addition of 1.5 μL APTES.[81] The synthesis conditions of Hexagonal mMSNs is based on reported literature.[65] The RITC-APTES solution was incubated at room temperature for at least 1 h. Next, 290 mg of CTAB was dissolved in 150 mL of 0.51 M ammonium hydroxide solution in a 250 mL beaker, sealed with parafilm (Neenah, WI), and placed in a mineral oil bath at 50 ^{o}C. After continuously stirring for 1 h, 3 mL of 0.88 M TEOS solution (prepared in ethanol) and 1 mL of RITC-APTES solution were combined and added immediately to the surfactant solution. After another 1 h of continuous stirring, the particle solution was stored at 50 ^{o}C for ~18 h under static conditions. Next, solution was passed through a 1.0 μm Acrodisc 25 mm syringe filter (PALL Life Sciences, Ann Arbor, MI) followed by a hydrothermal treatment at 70 ^{o}C for 24 h. Followed procedure for CTAB removal was as described in literature.[63] Briefly, mMSNs were transferred to 75 mM ammonium nitrate solution (prepared in ethanol) then placed in an oil bath at 60 ^{o}C for 1 h with reflux and stirring. The mMSNs were then washed in 95% ethanol and transferred to 12 mM HCl ethanolic solution and heated at 60 °C for 2 h with reflux and stirring. Lastly, Hexagonal mMSNs were washed in 95% ethanol, then 99.5% ethanol, and stored in 99.5% ethanol.

Synthesis of spherical mMSNs with isotropic pores (2.8 nm pore size). To prepare monosized spherical mMSNs composed of isotropic mesopores, we used the same procedure described above for synthesis of mMSNs with hexagonally arranged pore structure. However, we substituted cationic surfactant BDHAC for CTAB as the template. The 3-dimensional isotropic pore arrangement is due to a larger micelle packing parameter of BDHAC, compared to CTAB surfactant.[66]

Synthesis of spherical mMSNs composed of dendritic large pores (5 nm, 9 nm, and 18 nm pore size). The large pore spherical mMSNs were synthesized by a published biphase method.[67-69]

Syntheses of 5 nm, 9 nm, and 18 nm pore mMSNs are based on a modified condition reported by Zhao *et al*.[69] For preparation of 5 nm dendritic pore mMSNs, 0.18 g of TEA was dissolved in 36 mL of DI water and 24 mL of 25 w% CTAC in a 100 mL round bottom flask. The surfactant solution was stirred at 150 rpm and heated at 50 ^{o}C in an oil bath. After 1 h, 20 mL of 20 v/v % TEOS (in cyclohexane) was added to the CTAC-TEA aqueous solution. After 12 h, the particle solution was washed with DI water twice by centrifugation. Further surfactant removal achieved by following the previously described conditions used in preparation of small pore mMSNs. For synthesis of 9 nm dendritic pore mMSNs, the stirring rate and organic phase concentration were adjusted to 300 rpm and 10 v/v % TEOS, respectively. For synthesis of 18 nm dendritic pore mMSNs, the TEOS concentration in the organic phase was changed to 5 v/v %. All other steps were identical.

Synthesis of rod-shaped mMSNs with hexagonally arranged cylindrical pores (2.8 nm pore size). The shape of mMSNs can be simply tuned to rod-like morphology by altering the CTAB concentration, stirring rate, and ammonia concentration.[70, 71] Briefly, 0.5 g CTAB was dissolved in 150 mL of 0.22 M ammonium hydroxide solution at 25 ^{o}C under continuous stirring (300 rpm). Next, of 1 mL TEOS was added (drop wise) to the surfactant solution with stirring. After 1 h, the particle solution was aged under static conditions for 24 h, then subsequently transferred to a sealed container and heated to 70 ^{o}C for 24 h. The removal of surfactant was followed the same procedures described previously.

Liposome preparation. Lipids and chol ordered from Avanti Polar Lipids were presolubilized in chloroform at 25 mg/mL and were stored at -20 ^{o}C. To prepare liposomes, lipids were mixed at different mol% ratios including (54/44/2) for DOPC/chol/DOPE-PEG_{2000} and DSPC/chol/DSPE-PEG_{2000}, and (49/49/2) for DSPC/chol/DSPE-PEG_{2000}-NH_2 (Table S1). Lipid films were

prepared by drying lipid mixtures (in chloroform) under high vacuum to remove the organic solvent. Then the lipid film was hydrated in 0.5X PBS and bath sonicated for 30 minutes to obtain a liposome solution. Finally, the liposome solution was further passed through a 0.05 μm polycarbonate filter membrane (minimum 21 passes) using a mini-extruder to produce uniform and unilamellar vesicles with hydrodynamic diameters less than 100 nm.

Protocell assembly. To form protocells, mMSNs are transferred to D.I. water at 1 mg/mL concentration by centrifugation (15,000g, 10 minutes) and added to liposome solution (2 mg/mL) in 0.5X PBS (1:1 v/v and 1:2 w/w ratios). The mixture was bath sonicated ~ 10 s and non-fused liposomes were removed by centrifugation (15,000g, 10 minutes). Pelleted protocells were redispersed in 1X PBS *via* bath sonication, this step is repeated twice.

Anti-EGFR protocell preparation. First, DSPC/chol/DSPE-PEG-NH_2 liposomes were prepared according to the method described previously. Next, a ratio (2:1, w:w) of DSPC/chol/DSPE-PEG_{2000}-NH_2 liposomes to bare fluorescent-labeled Hexagonal mMSN were combined in a conical tube at room temperature for 30 minutes. The excess liposomes were removed by centrifugation (15,000 g, 10 minutes). The pelleted protocells were redispersed in 1 mL of PBS with bath sonication. To convert the surface -NH_2 to -SH groups, 50 μL of freshly prepared Traut's reagent (250 mM in PBS) was added to the protocells. After 1 h, the particles were centrifuged, and the supernatant was removed. The particles were again redispersed in 1 mL of PBS. Then, 0.15 mg of maleimide-activated NeutrAvidin protein was added to 0.25 mL of thiolated protocells and incubated at room temperature for 12 h. The NeutrAvidin conjugated protocells were washed with PBS *via* centrifugation and suspended in 0.25 mL of PBS. Then, 50 μL of biotinlyated EGFR antibody (0.1 mg/mL) was mixed with 50 μL of NeutrAvidin

conjugated protocells for at least 30 minutes. Finally, the antibody conjugated protocells were pelleted and redispersed in 100 μL PBS for *in vitro* targeting experiments.

Protocell biocompatibility assessment. Whole human blood was acquired from healthy donors with informed consent and stabilized in K_2EDTA tubes (BD Biosciences). hRBCs were purified following reported procedure,[100] then incubated with either bare mMSNs or protocells (25, 50, 100, 200, and 400 μg/mL) at 37 ^{o}C. After 3 h of exposure, samples were centrifuged at 300g for 3 minutes, then 100 μL of supernatant from each sample was transferred to a 96-well plate. Hemoglobin absorbance was measured using a BioTek microplate reader (Winooski, VT) at 541 nm. The percent hemolysis of each sample was quantified using a reported equation.[100] In addition, we examined the biocompatibility of anti-EGFR targeted protocells *in vitro*. We incubated ~1.5x10^5 cells/mL of REH and REH-EGFR cell lines with either 12.5, 25, 50, 100, and 200 μg/mL of anti-EGFR targeted protocells in complete medium for 1 h at 37 °C. Cells were washed twice in complete media and transferred to a 96-well plate for 24 h at 37 °C. Cell viability was assessed by CellTiter-Glo® 2.0 Assay as measured by BioTek microplate reader. The cell viability was calculated as a percentage of non-protocell treated sample.

Cell culture and nanoparticle nonspecific binding/uptake. Human endothelial cells, EA.hy926 (CRL-2922) were purchased from American Type Culture Center (ATCC, Manassas, VA). We seeded 5×10^5 EA.hy926 cells in 6-well plates with 2 mL of DMEM + 10% FBS and 1% PS at 37 ^{o}C in 5% CO_2 humidified atmosphere. After 24 h, the media was removed and replaced with 2 mL of fresh complete media supplemented with 20 μg/mL of bare mMSNs or protocells for 4 h at 37 ^{o}C under 5% CO_2. After nanoparticle incubation, the media was removed and the cells were gently washed twice with PBS. For imaging purposes, the nanoparticle treated cells were fixed in 3.7% formaldehyde (in PBS) at room temperature for 10 minutes, washed with PBS, then treated

with 0.1% Triton X-100 for another 10 minutes. The fixed cells were washed with PBS and stored in 1 mL of PBS. The cell nuclei and F-actin were stained with 1 mL of Hoechst 33342 (3.2 μM in PBS) and 0.5 mL of Alexa Fluor®488 phalloidin (20 nM in PBS) for 20 minutes, respectively. After staining, the cells were washed with PBS twice and stored in PBS prior to fluorescence microscope imaging. For preparation of flow cytometry samples, the control and nanoparticle treated cells were removed from plate bottom using Trypsin-EDTA (0.25%). The suspended cells were centrifuged, washed with PBS, and suspended in PBS for flow cytometry measurements.

Cell-nanoparticle interactions in ex ovo avian embryos. Ex ovo avian embryos were handled according to published methods,[92] with all experiments conducted following an institutional approval protocol (11-100652-T-HSC). This method included incubation of fertilized eggs (purchased from East Mountain Hatchery-Edgewood, NM) in a GQF 1500 Digital Professional egg incubator (Savannah, GA) for 3-4 days. Following initial *in ovo* incubation, embryos were removed from shells by cracking into 100 mL polystyrene weigh boats (VWR, Radnor, PA). *Ex ovo* embryos were then covered and incubated (~39 ^{o}C) with constant humidity (~70%). For nanoparticle injections, ~50 μg (at 1 mg/mL) of bare mMSNs or protocells in PBS were injected into secondary or tertiary veins of the CAM *via* pulled glass capillary needles. CAM vasculature and fluorescent protocells were imaged using a customized avian embryo chamber (humidified) and a Zeiss AxioExaminer upright microscope modified with a heated stage. High speed videos were acquired on the same microscope using a Hamamatsu Orca Flash 4.0 camera.

Post-circulation size and stability analyses. All animal care and experimental protocols were in accordance with the National Institutes of Health and University of New Mexico School of Medicine guidelines. Ten- to twelve-week-old female BALB/c mice (Charles River Laboratories,

Wilmington, MA) were administered dose of fluorescent protocells (10 mg/mL) in 150 µL PBS *via* tail vein injection. After 10 minutes of circulation, mice were euthanized and blood was drawn by cardiac puncture. Whole blood was stabilized in K_2EDTA microtainers (BD Biosciences) prior to analysis. *Ex ovo* avian embryos were administered dose of fluorescent protocells (1 mg/mL) in 50 µL PBS *via* secondary or tertiary veins of the CAM. After 10 minutes of circulation, blood was drawn *via* pulled glass capillary needles and analyzed immediately. Whole blood cells and protocell fluorescence in both mouse and avian samples were imaged on a glass slide with Zeiss AxioExaminer fixed stage microscope (Gottingen, Germany). To separate protocells from whole blood, samples were centrifuged at low speed to remove blood cells, supernatant fraction was transferred to a fresh tube then centrifuged at 15,000g for 10 minutes. The pellets were washed (15,000g for 10 minutes) twice in PBS, then protocell size was analyzed on Malvern Zetasizer Nano-ZS equipment.

In vitro targeting comparison of REH and REH-EGFR cell lines. The human leukemia cell lines, REH and REH-EGFR[96] were a kind gift from Professor David F. Stern, Yale University. The REH and REH-EGFR cells were suspended in RPMI 1640 supplemented with 10% FBS media at a concentration of ~$5x10^5$ cells/mL. Then one mL of cells was incubated with either NeutrAvidin terminated protocells or anti-EGFR protocells at 10 µg/mL for 5, 15, 30, and 60 minutes respectively at 37 ^oC under 5% CO_2. The nanoparticle-treated cells were pelleted using a benchtop centrifuge, washed with PBS twice. Cells were fixed in 4% paraformaldehyde for 5 minutes, then washed in PBS, then permeabilized with 0.1% Triton X100 for 5 minutes. The cell cytoskeleton and nuclei were stained by 0.1 mM of Alexa Fluor®488 phalloidin in PBS for 15 minutes, then washed in PBS, followed by 1.6 µM Hoechst 33342 in PBS for 10 minutes, followed by a final wash in PBS. Stained cells were imaged on a glass slide using the Zeiss

AxioExaminer upright microscope. Binding quantification of targeted protocells was determined by a fluorescence shift measured by a BD Accuri™ C6 flow cytometer.

Single cell targeting and model drug delivery in chicken embryos. First, ~1x10^7 of either REH or REH-EGFR cells were suspended in 1 mL PBS and incubated with 2 μL of CellTracker™ green CMFDA dye (2.7 mM in DMSO) for 10 minutes at 37 ^oC. The stained cells were centrifuged, washed, and suspended in 500 μL of PBS. Next, 50 μL of cell solution was administered to *ex ovo* avian embryos *via* the previously described procedure. After 30 minutes cell circulation, the anti-EGFR protocells (100 μL, 0.2 mg/mL) were injected into embryos intravenously. Binding of targeted protocells was assessed by fluorescence microscopy at 1, 4, and 9 h using the Zeiss AxioExaminer upright microscope. To assess internalization and cargo delivery, REH-EGFR cells were stained with CellTracker™ Blue CMAC dye and injected as described above, followed by injection of YO-PRO®-1 loaded RITC labelled protocells (50 μL, 1 mg/mL). Prior to imaging of we injected with DyLight 645 Len Culinaris Agglutin lectin stain to visualize the vasculature, we then imaged the binding, internalization, and cargo release by fluorescence microscopy at 4 and 16 h using the Zeiss AxioExaminer upright microscope.

Characterization. TEM images were acquired on a JEOL 2010 (Tokyo, Japan) equipped with a Gatan Orius digital camera system (Warrendale, PA) under a 200 kV voltage. The Cryo-TEM samples were prepared using an FEI Vitrobot Mark IV (Eindhoven, Netherlands) on Quantifoil® R1.2/1.3 holey carbon grids (sample volume of 4 μL, a blot force of 1, and blot and drain times of 4 and 0.5 seconds, respectively). Imaging was taken with a JEOL 2010 TEM at 200 kV using a Gatan model 626 cryo stage. Nitrogen adsorption-desorption isotherms of mMSNs were obtained from on a Micromeritics ASAP 2020 (Norcross, GA) at 77 K. Samples were degassed at 120 ^oC for 12 h before measurements. The surface area and pore size was calculated following

the Brunauer-Emmet-Teller (BET) equation in the range of P/P_o from 0.05 to 0.1 and standard Barrett-Joyer-Halenda (BJH) method. Flow cytometry data were performed on a Becton-Dickinson FACScalibur flow cytometer (Sunnyvale, CA). The raw data obtained from the flow cytometer was processed with FlowJo software (Tree Star, Inc. Ashland, OR). Hydrodynamic size and zeta potential data were acquired on a Malvern Zetasizer Nano-ZS equipped with a He-Ne laser (633 nm) and Non-Invasive Backscatter optics (NIBS). All samples for DLS measurements were suspended in various media (DI, PBS, and DMEM+10% FBS) at 1 mg/mL. Measurements were acquired at 25 ^{o}C or 37 ^{o}C. DLS measurements for each sample were obtained in triplicate. The Z-average diameter was used for all reported hydrodynamic size measurements. The zeta potential of each sample was measured in 1xPBS using monomodal analysis. All reported values correspond to the average of at least three independent samples. The fluorescence images were captured with a Zeiss AxioExaminer fixed stage microscope (Gottingen, Germany).

In vitro targeting comparison of Ba/F3 and Ba/F3-EGFR cell lines. The murine precursor B cell acute lymphoblastic leukemia (ALL) cell lines, Ba/F3 and Ba/F3-EGFR[96] were a kind gift from Professor David F. Stern, Yale University. The Ba/F3 and Ba/F3-EGFR cells were suspended in RPMI 1640 supplemented with 10% FBS media at a concentration of ~1x10^6 cells/mL. Then one mL of cells was incubated with anti-EGFR protocells at 5 μg/mL for 1 h at 37 ^{o}C under 5% CO_2. The cell nuclei and membrane were stained by 1 μL of Hoechst 33342 (1.6 mM in DI) and 2 μL of CellTracker™ green CMFDA dye (2.7 mM in DMSO) for 10 minutes. The nanoparticle-treated cells were pelleted using a benchtop centrifuge, washed with PBS twice, and dispersed in PBS. The live cells were imaged on a glass slide using the Zeiss AxioExaminer upright microscope. To further examine the specificity of targeted protocells, the binding of particles

was determined by a fluorescence shift measured by a Becton-Dickinson FACScalibur flow cytometer.

Cargo loading and release kinetics. Model drug loading was achieved by adding 1% volume YO-PRO®-1 (1 mM in DMSO) to mMSNs (1 mg/mL in H_2O) and stored for 12 h at 4 °C. After loading, targeted protocells were prepared using method described earlier in Anti-EGFR targeted protocell preparation. We observed a color change in the pelleted YO-PRO®-1 loaded protocells and did not observe any color in the supernatant during protocell assembly. We suspect that the interaction between YO-PRO®-1 and mMSNs to be largely driven by electrostatics, since YO-PRO®-1 carries a positive charge. Moreover, YO-PRO®-1 is membrane impermeable, therefore, it should remain encapsulated by the SLB of the protocell until it is broken down in the intracellular environment. To quantify YO-PRO®-1 loading, protocells were pelleted by centrifugation and resuspended in DMSO with bath sonication, this step was repeated twice. Supernatants were pooled and concentration was determined using a microplate reader fluorescence measurement at 480/510 nm. We calculated a mean 25% loading efficiency of YO-PRO®-1 for protocells used in the model drug delivery experiments *in vitro* and *ex ovo*. To load and quantify gemcitabine (GEM), 0.5 mg of Hexagonal mMSNs (m_{mMSN}) were suspended in 50 µL of GEM dissolved in DI water at 10 mg/mL (m_{GEM} = 0.5 mg) and stored for 12 h at 4 °C. After drug loading, targeted protocells were prepared using method described earlier in Anti-EGFR targeted protocell preparation. At each step, supernatant was collected, pooled (v_1 = 2.55 mL), and GEM loading was determined using a microplate reader absorbance measurement at 265 nm. A standard curve generated from a serial dilution of GEM in PBS (n = 3) was used to calculate the concentration of GEM in the supernatant. To account for absorbance signal from non-GEM components in the supernatant, unloaded protocells were prepared simultaneously

under identical conditions and measured at 265 nm. This absorbance value ($Abs_{control}$) was subtracted from the value obtained from supernatant containing GEM (Abs_{GEM}) prior to calculation of GEM concentration based on standard curve [c_1 = (Abs – 0.0507) / 7.7115]. For example, we used (m_{mMSN} = 0.5 mg), and (m_{GEM} = 0.5 mg) and we obtained (Abs_{GEM} = 2.51) and ($Abs_{control}$ = 1.18). To solve for the amount loaded [$Abs_{GEM} - Abs_{control}$] = 1.33, then GEM amount in the supernatant can be calculated by [c_1 = (1.33 – 0.0507) / 7.7115] = 0.17 mg/mL. The total volume of the pooled supernatant is used to calculate the amount of GEM in the supernatant (m_1 = c_1 * v_1) or (m_1 = 0.17 mg/ml * 2.55 mL) = 0.43 mg. The supernatant amount (m_1) was then subtracted from the starting GEM amount (m_{GEM}) to estimate the total amount loaded into protocells [$m_{loaded} = m_0 - m_1$] or (0.5 mg – 0.43 mg) = 0.07 mg. To estimate the loading capacity as a percentage of weight we use the formula [(m_{loaded} / m_{mMSN}) * 100%] or (0.07 mg / 0.5 mg) * 100% = 14% (w/w). This experiment was repeated 4 times with different Hexagonal mMSN preparations and we determined the average GEM loading capacity of protocell = 15.25% ± 1.6% (mean ± SD). While the loading percentage of our protocells is lower than what was reported by Dr. Nel's group, our loading conditions contain half the amount of GEM that was described by the Meng *et.al*.[39] Since GEM is neutral at physiological pH, and mMSNs are negatively charged, we do not suspect an electrostatic interaction to play a significant role in loading, instead suspect the GEM and mMSNs will reach an equilibrium state where the small molecule drug will occupy the high internal space of the pores and will then be encapsulated with the addition of the lipid bilayer in protocell assembly. We used a 3.5-5 kD MWCO Float-A-Lyzer to evaluate GEM release kinetics in either PBS (pH 7.4) or citrate buffer (pH 5.0). GEM was encapsulated into protocells as described above, then protocells were loaded into Float-A-lyzers and sealed in 50 mL conical tubes containing either PBS or citrate buffer, and stored at

37°C while stirring. We removed 0.5 mL of dialysate for 265 nm absorbance analysis on a BioTek microplate reader at multiple time points, then added 0.5 mL of fresh dialysate solution to the conical tube. To assess protocell size at 24 and 72 h we removed sample from the Float-a-Lyzer, and measured the hydrodynamic size on Malvern Zetasizer Nano ZS, then placed back inside the Float-a-Lyzer and stored at 37°C while stirring. Consistent with findings reported by Meng *et.al*,[39] we did not see evidence of drug precipitation and we determined the effective release of GEM by cell viability analysis, in addition, our loaded and targeted protocell maintained monodispersity.

Targeted protocell GEM delivery and cytotoxicity assessment. We incubated ~$1.5x10^5$ cells/mL of REH and REH-EGFR cell lines with either 0, 1, 5, 10, 25, or 50 μg/mL of GEM loaded (~15% w/w) anti-EGFR targeted protocells in complete medium for 1 h at 37 °C. Cells were centrifuged (500g, 3 minutes) and washed twice in complete media and transferred to a white 96-well plate for 24 h at 37 °C. In comparison, we incubated ~$1.5x10^5$ cells/mL of REH and REH-EGFR cell lines with either 0, 0.6, 3, 6, 15, or 30 μM of free GEM, the equivalent doses based on 15% (w/w) GEM loading into protocells, under identical experimental conditions. Cell viability was assessed by CellTiter-Glo® 2.0 Assay as measured by BioTek microplate reader. The cell viability was calculated as a percentage of non-protocell treated sample.

In vitro internalization and cargo release assay. REH-EGFR cells were suspended in RPMI 1640 supplemented with 10% FBS media at a concentration of $5x10^5$ cells/mL. Then one mL of cells was incubated with YO-PRO®-1 loaded, RITC-labelled anti-EGFR protocells at 10 μg/mL for 60 minutes at 37 °C, washed twice in media to remove unbound protocells, and incubated for 1, 8, 16, and 24 h respectively at 37 $^{\circ}$C under 5% CO_2. The protocell-treated cells were pelleted using a benchtop centrifuge, at each time point, and resuspended in an acid wash solution (0.2 M

acetic acid, 0.5 M NaCl, pH 2.8) and incubated on ice for 5 minutes. Cells were then washed twice with PBS by centrifugation and protocell internalization was assessed by a red fluorescence shift and cargo release was assessed by a green fluorescence shift as measured by a BD Accuri™ C6 flow cytometer. Additionally, live cells were imaged on a glass slide using the Leica DMI3000 B inverted microscope.

ASSOCIATED CONTENT

Supporting Information. Additional data, experimental details, and videos. This material is available free of charge *via* the Internet at http://pubs.acs.org

AUTHOR INFORMATION

Corresponding Authors

*E-mail: linxx484@umn.edu; *E-mail: cjbrink@sandia.gov

Present Addresses

◆ Oncothyreon Inc, 2601 Fourth Avenue, Seattle, WA, USA 98121-3222;

■ Sandia National Laboratories, Advanced Materials Laboratory, 1001 University Blvd. SE, Suite 100, Albuquerque, NM, USA 87106

Author Contributions

The manuscript was written through contributions of all authors. All authors have given approval to the final version of the manuscript.

ACKNOWLEDGMENTS

We thank Dr. David F. Stern, Department of Pathology, Yale University for the gift of the EGFR retroviral construct and Dr. Darryl Y. Sasaki, Biotechnology and Bioengineering Department, Sandia National Laboratories, and Dr. Atul N. Parikh, Department of Biomedical Engineering, The University of California Davis, for useful comments and discussions. Cryo-TEM images of EISA protocells were carried out at Baylor College of Medicine (Houston, TX) by C. Jia-Yin Fu, H. Khant and W. Chiu. This work was supported by the NIH National Cancer Institute (NCI) Grant UO1 CA151792-01, the Leukemia and Lymphoma Society (LLS) Specialized Center of Research (SCOR) Award 7010-14, and the Sandia National Laboratories Laboratory Directed Research and Development (LDRD) program. P.N.D. and Y.S.L. were funded by a fellowship from the New Mexico Cancer Nanoscience and Microsystems Training Center (CNTC). P.N.D. was also supported by the George D. Montoya Research Scholarship, Edmund J. & Thelma W. Evans Charitable Trust Scholarship, and the Charlotte and William Kraft Graduate Fellowship. J.L.T. was supported by a Young Investigators Award from Gabrielle's Angel Foundation. A.J.L. was supported by the UNM Science, Technology, Engineering and Mathematics (STEM) Talent Expansion Program. A.J.M. was supported by a grant from the National Institute of General Medical Sciences award # T34GM008751. K.R.H. was supported by the UNM NSMS Research Experience for Undergraduates Program. C.J.B. and S.C. acknowledge the U.S. Department of Energy (DOE), Office of Basic Energy Sciences (BES), Division of Materials Sciences and Engineering, for support of fundamental structure-property relationship studies. C.J.B. further acknowledges the Air Force Office of Scientific Research grant FA 9550-1-14-066, the National Science Foundation Grant #1344298, and the University of California's Center for Environmental Implications of Nanotechnology (CEIN) Grant # DBI-1266377. This research

also utilized critical Shared Resources in the UNM Comprehensive Cancer Center (Fluorescence Microscopy and Cell Imaging; Biostatistics; Flow Cytometry and High Throughput Screening) supported by NCI P30 CA118110.

ToC Graphic

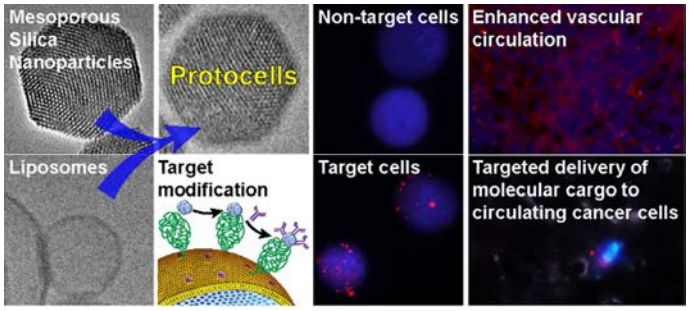

REFERENCES

1. Bertrand, N.; Wu, J.; Xu, X.; Kamaly, N.; Farokhzad, O. C. Cancer Nanotechnology: The Impact of Passive and Active Targeting in the Era of Modern Cancer Biology. *Adv. Drug Delivery Rev.* 2014, 66, 2-25.
2. Sun, T.; Zhang, Y. S.; Pang, B.; Hyun, D. C.; Yang, M.; Xia, Y. Engineered Nanoparticles for Drug Delivery in Cancer Therapy. *Angew. Chem., Int. Ed.* 2014, 53, 12320-12364.
3. Tarn, D.; Ashley, C. E.; Xue, M.; Carnes, E. C.; Zink, J. I.; Brinker, C. J. Mesoporous Silica Nanoparticle Nanocarriers: Biofunctionality and Biocompatibility. *Acc. Chem. Res.* 2013, 46, 792-801.
4. Padera, T. P.; Stoll, B. R.; Tooredman, J. B.; Capen, D.; Tomaso, E. d.; Jain, R. K. Pathology: Cancer Cells Compress Intratumour Vessels. *Nature* 2004, 427, 695-695.
5. Chauhan, V. P.; Stylianopoulos, T.; Martin, J. D.; Popovic, Z.; Chen, O.; Kamoun, W. S.; Bawendi, M. G.; Fukumura, D.; Jain, R. K. Normalization of Tumour Blood Vessels Improves the Delivery of Nanomedicines in a Size-Dependent Manner. *Nat. Nanotechnol.* 2012, 7, 383-388.
6. Blanco, E.; Shen, H.; Ferrari, M. Principles of Nanoparticle Design for Overcoming Biological Barriers to Drug Delivery. *Nat. Biotechnol.* 2015, 33, 941-951.
7. Peer, D.; Karp, J. M.; Hong, S.; Farokhzad, O. C.; Margalit, R.; Langer, R. Nanocarriers as an Emerging Platform for Cancer Therapy. *Nat. Nanotechnol.* 2007, 2, 751-760.
8. Bartlett, D. W.; Su, H.; Hildebrandt, I. J.; Weber, W. A.; Davis, M. E. Impact of Tumor-Specific Targeting on the Biodistribution and Efficacy of Sirna Nanoparticles Measured by Multimodality *in Vivo* Imaging. *Proc. Natl. Acad. Sci. U. S. A.* 2007, 104, 15549-15554.
9. Bae, Y. H. Drug Targeting and Tumor Heterogeneity. *J. Controlled Release* 2009, 133, 2-3.
10. Lammers, T.; Kiessling, F.; Hennink, W. E.; Storm, G. Drug Targeting to Tumors: Principles, Pitfalls and (Pre-) Clinical Progress. *J. Controlled Release* 2012, 161, 175-187.
11. Shi, J.; Xiao, Z.; Kamaly, N.; Farokhzad, O. C. Self-Assembled Targeted Nanoparticles: Evolution of Technologies and Bench to Bedside Translation. *Acc. Chem. Res.* 2011, 44, 1123-1134.
12. Iyer, A. K.; Singh, A.; Ganta, S.; Amiji, M. M. Role of Integrated Cancer Nanomedicine in Overcoming Drug Resistance. *Adv. Drug Delivery Rev.* 2013, 65, 1784-1802.

13. Markman, J. L.; Rekechenetskiy, A.; Holler, E.; Ljubimova, J. Y. Nanomedicine Therapeutic Approaches to Overcome Cancer Drug Resistance. *Adv. Drug Delivery Rev.* 2013, 65, 1866-1879.
14. Adamson, P. C. Improving the Outcome for Children with Cancer: Development of Targeted New Agents. *Ca-Cancer J. Clin.* 2015, 65, 212-220.
15. Krishnan, V.; Rajasekaran, A. K. Clinical Nanomedicine: A Solution to the Chemotherapy Conundrum in Pediatric Leukemia Therapy. *Clin. Pharmacol. Ther.* 2014, 95, 168-178.
16. Allen, T. M.; Cullis, P. R. Drug Delivery Systems: Entering the Mainstream. *Science* 2004, 303, 1818-1822.
17. Iwamoto, T. Clinical Application of Drug Delivery Systems in Cancer Chemotherapy: Review of the Efficacy and Side Effects of Approved Drugs. *Biol. Pharm. Bull.* 2013, 36, 715-718.
18. Egusquiaguirre, S.; Igartua, M.; Hernández, R.; Pedraz, J. Nanoparticle Delivery Systems for Cancer Therapy: Advances in Clinical and Preclinical Research. *Clin. Transl. Oncol.* 2012, 14, 83-93.
19. Pattni, B. S.; Chupin, V. V.; Torchilin, V. P. Chem. Rev. *Chemical Reviews* 2015, 115, 10938-10966.
20. Davis, M. E.; Chen, Z.; Shin, D. M. Nanoparticle Therapeutics: An Emerging Treatment Modality for Cancer. *Nat Rev Drug Discov* 2008, 7, 771-782.
21. Deshpande, P. P.; Biswas, S.; Torchilin, V. P. Current Trends in the Use of Liposomes for Tumor Targeting. *Nanomedicine (London, U. K.)* 2013, 8, 10.2217/nnm.13.118.
22. Farokhzad, O. C.; Langer, R. Acs Nano. *ACS Nano* 2009, 3, 16-20.
23. Torchilin, V. P. Recent Advances with Liposomes as Pharmaceutical Carriers. *Nat. Rev. Drug Discovery* 2005, 4, 145-160.
24. Çağdaş, M.; Sezer, A. D.; Bucak, S. Liposomes as Potential Drug Carrier Systems for Drug Delivery. INTECH: 2014.
25. Reynolds, J. G.; Geretti, E.; Hendriks, B. S.; Lee, H.; Leonard, S. C.; Klinz, S. G.; Noble, C. O.; Lücker, P. B.; Zandstra, P. W.; Drummond, D. C.; Olivier Jr, K. J.; Nielsen, U. B.; Niyikiza, C.; Agresta, S. V.; Wickham, T. J. Her2-Targeted Liposomal Doxorubicin Displays Enhanced Anti-Tumorigenic Effects without Associated Cardiotoxicity. *Toxicol. Appl. Pharmacol.* 2012, 262, 1-10.
26. Elsabahy, M.; Wooley, K. L. Design of Polymeric Nanoparticles for Biomedical Delivery Applications. *Chem. Soc. Rev.* 2012, 41, 2545-2561.
27. Draz, M. S.; Fang, B. A.; Zhang, P.; Hu, Z.; Gu, S.; Weng, K. C.; Gray, J. W.; Chen, F. F. Nanoparticle-Mediated Systemic Delivery of Sirna for Treatment of Cancers and Viral Infections. *Theranostics* 2014, 4, 872-892.
28. Williford, J.-M.; Wu, J.; Ren, Y.; Archang, M. M.; Leong, K. W.; Mao, H.-Q. Recent Advances in Nanoparticle-Mediated Sirna Delivery. *Annu. Rev. Biomed. Eng.* 2014, 16, 347-370.
29. Li, Z.; Barnes, J. C.; Bosoy, A.; Stoddart, J. F.; Zink, J. I. Mesoporous Silica Nanoparticles in Biomedical Applications. *Chem. Soc. Rev.* 2012, 41, 2590-2605.
30. Vivero-Escoto, J. L.; Slowing, I. I.; Trewyn, B. G.; Lin, V. S. Y. Mesoporous Silica Nanoparticles for Intracellular Controlled Drug Delivery. *Small* 2010, 6, 1952-1967.
31. Butler, K. S.; Durfee, P. N.; Theron, C.; Ashley, C. E.; Carnes, E. C.; Brinker, C. J. Protocells: Modular Mesoporous Silica Nanoparticle-Supported Lipid Bilayers for Drug Delivery. *Small* 2016.

32. Zhang, H.; Dunphy, D. R.; Jiang, X.; Meng, H.; Sun, B.; Tarn, D.; Xue, M.; Wang, X.; Lin, S.; Ji, Z.; Li, R.; Garcia, F. L.; Yang, J.; Kirk, M. L.; Xia, T.; Zink, J. I.; Nel, A.; Brinker, C. J. Processing Pathway Dependence of Amorphous Silica Nanoparticle Toxicity: Colloidal *Vs* Pyrolytic. *J. Am. Chem. Soc.* 2012, 134, 15790-15804.
33. Meng, H.; Yang, S.; Li, Z.; Xia, T.; Chen, J.; Ji, Z.; Zhang, H.; Wang, X.; Lin, S.; Huang, C.; Zhou, Z. H.; Zink, J. I.; Nel, A. E. Aspect Ratio Determines the Quantity of Mesoporous Silica Nanoparticle Uptake by a Small Gtpase-Dependent Macropinocytosis Mechanism. *ACS Nano* 2011, 5, 4434-4447.
34. Brinker, C. J.; Scherer, G. W. *Sol-Gel Science: The Physics and Chemistry of Sol-Gel Processing*. Academic press: 2013.
35. Wang, L.-S.; Wu, L.-C.; Lu, S.-Y.; Chang, L.-L.; Teng, I. T.; Yang, C.-M.; Ho, J.-a. A. Biofunctionalized Phospholipid-Capped Mesoporous Silica Nanoshuttles for Targeted Drug Delivery: Improved Water Suspensibility and Decreased Nonspecific Protein Binding. *ACS Nano* 2010, 4, 4371-4379.
36. Ashley, C. E.; Carnes, E. C.; Epler, K. E.; Padilla, D. P.; Phillips, G. K.; Castillo, R. E.; Wilkinson, D. C.; Wilkinson, B. S.; Burgard, C. A.; Kalinich, R. M.; Townson, J. L.; Chackerian, B.; Willman, C. L.; Peabody, D. S.; Wharton, W.; Brinker, C. J. Delivery of Small Interfering Rna by Peptide-Targeted Mesoporous Silica Nanoparticle-Supported Lipid Bilayers. *ACS Nano* 2012, 6, 2174-2188.
37. Epler, K.; Padilla, D.; Phillips, G.; Crowder, P.; Castillo, R.; Wilkinson, D.; Wilkinson, B.; Burgard, C.; Kalinich, R.; Townson, J.; Chackerian, B.; Willman, C.; Peabody, D.; Wharton, W.; Brinker, C. J.; Ashley, C.; Carnes, E. Delivery of Ricin Toxin a-Chain by Peptide-Targeted Mesoporous Silica Nanoparticle-Supported Lipid Bilayers. *Adv. Healthcare Mater.* 2012, 1, 348-353.
38. Cauda, V.; Engelke, H.; Sauer, A.; Arcizet, D.; Bräuchle, C.; Rädler, J.; Bein, T. Colchicine-Loaded Lipid Bilayer-Coated 50 Nm Mesoporous Nanoparticles Efficiently Induce Microtubule Depolymerization Upon Cell Uptake. *Nano Lett.* 2010, 10, 2484-2492.
39. Meng, H.; Wang, M.; Liu, H.; Liu, X.; Situ, A.; Wu, B.; Ji, Z.; Chang, C. H.; Nel, A. E. Use of a Lipid-Coated Mesoporous Silica Nanoparticle Platform for Synergistic Gemcitabine and Paclitaxel Delivery to Human Pancreatic Cancer in Mice. *ACS Nano* 2015, 9, 3540-3557.
40. Wang, D.; Huang, J.; Wang, X.; Yu, Y.; Zhang, H.; Chen, Y.; Liu, J.; Sun, Z.; Zou, H.; Sun, D.; Zhou, G.; Zhang, G.; Lu, Y.; Zhong, Y. The Eradication of Breast Cancer Cells and Stem Cells by 8-Hydroxyquinoline-Loaded Hyaluronan Modified Mesoporous Silica Nanoparticle-Supported Lipid Bilayers Containing Docetaxel. *Biomaterials* 2013, 34, 7662-7673.
41. Zhang, X.; Li, F.; Guo, S.; Chen, X.; Wang, X.; Li, J.; Gan, Y. Biofunctionalized Polymer-Lipid Supported Mesoporous Silica Nanoparticles for Release of Chemotherapeutics in Multidrug Resistant Cancer Cells. *Biomaterials* 2014, 35, 3650-3665.
42. Ashley, C. E.; Carnes, E. C.; Phillips, G. K.; Padilla, D.; Durfee, P. N.; Brown, P. A.; Hanna, T. N.; Liu, J.; Phillips, B.; Carter, M. B.; Carroll, N. J.; Jiang, X.; Dunphy, D. R.; Willman, C. L.; Petsev, D. N.; Evans, D. G.; Parikh, A. N.; Chackerian, B.; Wharton, W.; Peabody, D. S.; Brinker, C. J. The Targeted Delivery of Multicomponent Cargos to Cancer Cells by Nanoporous Particle-Supported Lipid Bilayers. *Nat. Mater.* 2011, 10, 389-397.
43. Liu, X.; Situ, A.; Kang, Y.; Villabroza, K. R.; Liao, Y.; Chang, C. H.; Donahue, T.; Nel, A. E.; Meng, H. Irinotecan Delivery by Lipid-Coated Mesoporous Silica Nanoparticles Shows

Improved Efficacy and Safety over Liposomes for Pancreatic Cancer. *ACS Nano* 2016, 10, 2702-2715.
44. Huang, W.-C.; Burnouf, P.-A.; Su, Y.-C.; Chen, B.-M.; Chuang, K.-H.; Lee, C.-W.; Wei, P.-K.; Cheng, T.-L.; Roffler, S. R. Engineering Chimeric Receptors to Investigate the Size- and Rigidity-Dependent Interaction of Pegylated Nanoparticles with Cells. *ACS Nano* 2016, 10, 648-662.
45. Mackowiak, S. A.; Schmidt, A.; Weiss, V.; Argyo, C.; von Schirnding, C.; Bein, T.; Bräuchle, C. Targeted Drug Delivery in Cancer Cells with Red-Light Photoactivated Mesoporous Silica Nanoparticles. *Nano Lett.* 2013, 13, 2576-2583.
46. Porotto, M.; Yi, F.; Moscona, A.; LaVan, D. A. Synthetic Protocells Interact with Viral Nanomachinery and Inactivate Pathogenic Human Virus. *PloS one* 2011, 6, e16874.
47. Han, N.; Zhao, Q.; Wan, L.; Wang, Y.; Gao, Y.; Wang, P.; Wang, Z.; Zhang, J.; Jiang, T.; Wang, S. Hybrid Lipid-Capped Mesoporous Silica for Stimuli-Responsive Drug Release and Overcoming Multidrug Resistance. *ACS Appl. Mater. Interfaces* 2015, 7, 3342-3351.
48. Liu, J.; Stace-Naughton, A.; Jiang, X.; Brinker, C. J. Porous Nanoparticle Supported Lipid Bilayers (Protocells) as Delivery Vehicles. *J. Am. Chem. Soc.* 2009, 131, 1354-1355.
49. Liu, J.; Jiang, X.; Ashley, C.; Brinker, C. J. Electrostatically Mediated Liposome Fusion and Lipid Exchange with a Nanoparticle-Supported Bilayer for Control of Surface Charge, Drug Containment, and Delivery. *J. Am. Chem. Soc.* 2009, 131, 7567-7569.
50. Bayerl, T. M.; Bloom, M. Physical Properties of Single Phospholipid Bilayers Adsorbed to Micro Glass Beads. A New Vesicular Model System Studied by 2h-Nuclear Magnetic Resonance. *Biophys. J.* 1990, 58, 357-362.
51. Johnson, S. J.; Bayerl, T. M.; McDermott, D. C.; Adam, G. W.; Rennie, A. R.; Thomas, R. K.; Sackmann, E. Structure of an Adsorbed Dimyristoylphosphatidylcholine Bilayer Measured with Specular Reflection of Neutrons. *Biophys. J.* 1991, 59, 289-294.
52. Keller, C. A.; Glasmästar, K.; Zhdanov, V. P.; Kasemo, B. Formation of Supported Membranes from Vesicles. *Phys. Rev. Lett.* 2000, 84, 5443-5446.
53. Reviakine, I.; Brisson, A. Formation of Supported Phospholipid Bilayers from Unilamellar Vesicles Investigated by Atomic Force Microscopy. *Langmuir* 2000, 16, 1806-1815.
54. Johnson, J. M.; Ha, T.; Chu, S.; Boxer, S. G. Early Steps of Supported Bilayer Formation Probed by Single Vesicle Fluorescence Assays. *Biophys. J.* 2002, 83, 3371-3379.
55. Richter, R. P.; Brisson, A. R. Following the Formation of Supported Lipid Bilayers on Mica: A Study Combining Afm, Qcm-D, and Ellipsometry. *Biophys. J.* 2005, 88, 3422-3433.
56. Cremer, P. S.; Boxer, S. G. Formation and Spreading of Lipid Bilayers on Planar Glass Supports. *J. Phys. Chem. B* 1999, 103, 2554-2559.
57. Savarala, S.; Ahmed, S.; Ilies, M. A.; Wunder, S. L. Formation and Colloidal Stability of Dmpc Supported Lipid Bilayers on Sio2 Nanobeads. *Langmuir* 2010, 26, 12081-12088.
58. Garcia-Manyes, S.; Oncins, G.; Sanz, F. Effect of Ion-Binding and Chemical Phospholipid Structure on the Nanomechanics of Lipid Bilayers Studied by Force Spectroscopy. *Biophys. J.* 2005, 89, 1812-1826.
59. Mornet, S.; Lambert, O.; Duguet, E.; Brisson, A. The Formation of Supported Lipid Bilayers on Silica Nanoparticles Revealed by Cryoelectron Microscopy. *Nano Lett.* 2005, 5, 281-285.
60. Buranda, T.; Huang, J.; Ramarao, G.; Ista, L. K.; Larson, R. S.; Ward, T. L.; Sklar, L. A.; Lopez, G. P. Biomimetic Molecular Assemblies on Glass and Mesoporous Silica Microbeads for Biotechnology. *Langmuir* 2003, 19, 1654-1663.

61. Dengler, E. C.; Liu, J.; Kerwin, A.; Torres, S.; Olcott, C. M.; Bowman, B. N.; Armijo, L.; Gentry, K.; Wilkerson, J.; Wallace, J.; Jiang, X.; Carnes, E. C.; Brinker, C. J.; Milligan, E. D. Mesoporous Silica-Supported Lipid Bilayers (Protocells) for DNA Cargo Delivery to the Spinal Cord. *J. Controlled Release* 2013, 168, 209-224.
62. Marsh, D. *Handbook of Lipid Bilayers*. CRC Press: 2013.
63. Lin, Y.-S.; Abadeer, N.; Hurley, K. R.; Haynes, C. L. Ultrastable, Redispersible, Small, and Highly Organomodified Mesoporous Silica Nanotherapeutics. *J. Am. Chem. Soc.* 2011, 133, 20444-20457.
64. Lin, Y.-S.; Tsai, C.-P.; Huang, H.-Y.; Kuo, C.-T.; Hung, Y.; Huang, D.-M.; Chen, Y.-C.; Mou, C.-Y. Well-Ordered Mesoporous Silica Nanoparticles as Cell Markers. *Chem. Mater.* 2005, 17, 4570-4573.
65. Lin, Y.-S.; Haynes, C. L. Impacts of Mesoporous Silica Nanoparticle Size, Pore Ordering, and Pore Integrity on Hemolytic Activity. *J. Am. Chem. Soc.* 2010, 132, 4834-4842.
66. Chen, P.-K.; Lai, N.-C.; Ho, C.-H.; Hu, Y.-W.; Lee, J.-F.; Yang, C.-M. New Synthesis of Mcm-48 Nanospheres and Facile Replication to Mesoporous Platinum Nanospheres as Highly Active Electrocatalysts for the Oxygen Reduction Reaction. *Chem. Mater.* 2013, 25, 4269-4277.
67. Nandiyanto, A. B. D.; Kim, S.-G.; Iskandar, F.; Okuyama, K. Synthesis of Spherical Mesoporous Silica Nanoparticles with Nanometer-Size Controllable Pores and Outer Diameters. *Microporous Mesoporous Mater.* 2009, 120, 447-453.
68. Wang, J.; Sugawara-Narutaki, A.; Shimojima, A.; Okubo, T. Biphasic Synthesis of Colloidal Mesoporous Silica Nanoparticles Using Primary Amine Catalysts. *J. Colloid Interface Sci.* 2012, 385, 41-47.
69. Shen, D.; Yang, J.; Li, X.; Zhou, L.; Zhang, R.; Li, W.; Chen, L.; Wang, R.; Zhang, F.; Zhao, D. Biphase Stratification Approach to Three-Dimensional Dendritic Biodegradable Mesoporous Silica Nanospheres. *Nano Lett.* 2014, 14, 923-932.
70. Huang, X.; Li, L.; Liu, T.; Hao, N.; Liu, H.; Chen, D.; Tang, F. The Shape Effect of Mesoporous Silica Nanoparticles on Biodistribution, Clearance, and Biocompatibility *in Vivo*. *ACS Nano* 2011, 5, 5390-5399.
71. Yu, T.; Malugin, A.; Ghandehari, H. Impact of Silica Nanoparticle Design on Cellular Toxicity and Hemolytic Activity. *ACS Nano* 2011, 5, 5717-5728.
72. Sackmann, E. Membrane Bending Energy Concept of Vesicle- and Cell-Shapes and Shape-Transitions. *FEBS Lett.* 1994, 346, 3-16.
73. Henriksen, J.; Rowat, A. C.; Brief, E.; Hsueh, Y. W.; Thewalt, J. L.; Zuckermann, M. J.; Ipsen, J. H. Universal Behavior of Membranes with Sterols. *Biophysical Journal* 2006, 90, 1639-1649.
74. Sackmann, E. Physical Basis of Self-Organization and Function of Membranes: Physics of Vesicles. *Handbook of Biological Physics* 1995, 1, 213-304.
75. Yeagle, P. L. *The Structure of Biological Membranes*. CRC press: 2004.
76. Nollert, P.; Kiefer, H.; Jähnig, F. Lipid Vesicle Adsorption *Versus* Formation of Planar Bilayers on Solid Surfaces. *Biophys. J.* 1995, 69, 1447.
77. Seantier, B.; Kasemo, B. Influence of Mono- and Divalent Ions on the Formation of Supported Phospholipid Bilayers *Via* Vesicle Adsorption. *Langmuir* 2009, 25, 5767-5772.
78. Crist, R. M.; Grossman, J. H.; Patri, A. K.; Stern, S. T.; Dobrovolskaia, M. A.; Adiseshaiah, P. P.; Clogston, J. D.; McNeil, S. E. Common Pitfalls in Nanotechnology: Lessons Learned from Nci's Nanotechnology Characterization Laboratory. *Integr. Biol.* 2013, 5, 66-73.

79. Lin, Y.-S.; Hurley, K. R.; Haynes, C. L. Critical Considerations in the Biomedical Use of Mesoporous Silica Nanoparticles. *J. Phys. Chem. Lett.* 2012, 3, 364-374.
80. Zarschler, K.; Prapainop, K.; Mahon, E.; Rocks, L.; Bramini, M.; Kelly, P. M.; Stephan, H.; Dawson, K. A. Diagnostic Nanoparticle Targeting of He Egf-Receptor in Complex Biological Conditions Using Single-Domain Antibodies. *Nanoscale* 2014, 6, 6046-6056.
81. Townson, J. L.; Lin, Y.-S.; Agola, J. O.; Carnes, E. C.; Leong, H. S.; Lewis, J. D.; Haynes, C. L.; Brinker, C. J. Re-Examining the Size/Charge Paradigm: Differing *in Vivo* Characteristics of Size- and Charge-Matched Mesoporous Silica Nanoparticles. *J. Am. Chem. Soc.* 2013, 135, 16030-16033.
82. Lis, M.; Wizert, A.; Przybylo, M.; Langner, M.; Swiatek, J.; Jungwirth, P.; Cwiklik, L. The Effect of Lipid Oxidation on the Water Permeability of Phospholipids Bilayers. *Physical Chemistry Chemical Physics* 2011, 13, 17555-17563.
83. Estephan, Z. G.; Jaber, J. A.; Schlenoff, J. B. Zwitterion-Stabilized Silica Nanoparticles: Toward Nonstick Nano. *Langmuir* 2010, 26, 16884-16889.
84. Zhu, Y.; Sundaram, H. S.; Liu, S.; Zhang, L.; Xu, X.; Yu, Q.; Xu, J.; Jiang, S. A Robust Graft-to Strategy to Form Multifunctional and Stealth Zwitterionic Polymer-Coated Mesoporous Silica Nanoparticles. *Biomacromolecules* 2014, 15, 1845-1851.
85. Soo Choi, H.; Liu, W.; Misra, P.; Tanaka, E.; Zimmer, J. P.; Itty Ipe, B.; Bawendi, M. G.; Frangioni, J. V. Renal Clearance of Quantum Dots. *Nat. Biotechnol.* 2007, 25, 1165-1170.
86. Nag, O.; Awasthi, V. Surface Engineering of Liposomes for Stealth Behavior. *Pharmaceutics* 2013, 5, 542.
87. Breus, V. V.; Heyes, C. D.; Tron, K.; Nienhaus, G. U. Zwitterionic Biocompatible Quantum Dots for Wide Ph Stability and Weak Nonspecific Binding to Cells. *ACS Nano* 2009, 3, 2573-2580.
88. Ferrari, M. Nanogeometry: Beyond Drug Delivery. *Nat. Nanotechnol.* 2008, 3, 131-132.
89. Lu, Y.; Fan, H.; Stump, A.; Ward, T. L.; Rieker, T.; Brinker, C. J. Aerosol-Assisted Self-Assembly of Mesostructured Spherical Nanoparticles. *Nature* 1999, 398, 223-226.
90. Dobrovolskaia, M. A.; McNeil, S. E. Understanding the Correlation between *in Vitro* and *in Vivo* Immunotoxicity Tests for Nanomedicines. *J. Controlled Release* 2013, 172, 456-466.
91. Vargas, A.; Zeisser-Labouèbe, M.; Lange, N.; Gurny, R.; Delie, F. The Chick Embryo and Its Chorioallantoic Membrane (Cam) for the *in Vivo* Evaluation of Drug Delivery Systems. *Adv. Drug Delivery Rev.* 2007, 59, 1162-1176.
92. Leong, H. S.; Steinmetz, N. F.; Ablack, A.; Destito, G.; Zijlstra, A.; Stuhlmann, H.; Manchester, M.; Lewis, J. D. Intravital Imaging of Embryonic and Tumor Neovasculature Using Viral Nanoparticles. *Nat. Protoc.* 2010, 5, 1406-1417.
93. He, Q.; Zhang, Z.; Gao, F.; Li, Y.; Shi, J. *In Vivo* Biodistribution and Urinary Excretion of Mesoporous Silica Nanoparticles: Effects of Particle Size and Pegylation. *Small* 2011, 7, 271-280.
94. Asefa, T.; Tao, Z. Biocompatibility of Mesoporous Silica Nanoparticles. *Chem. Res. Toxicol.* 2012, 25, 2265-2284.
95. Lynch, I.; Dawson, K. A. Protein-Nanoparticle Interactions. *Nano Today* 2008, 3, 40-47.
96. Riese, D. J.; van Raaij, T. M.; Plowman, G. D.; Andrews, G. C.; Stern, D. F. The Cellular Response to Neuregulins Is Governed by Complex Interactions of the Erbb Receptor Family. *Mol. Cell. Biol.* 1995, 15, 5770-5776.

97. Federico, C.; Morittu, V. M.; Britti, D.; Trapasso, E.; Cosco, D. Gemcitabine-Loaded Liposomes: Rationale, Potentialities and Future Perspectives. *Int. J. Nanomed.* 2012, 7, 5423-5436.
98. de Sousa Cavalcante, L.; Monteiro, G. Gemcitabine: Metabolism and Molecular Mechanisms of Action, Sensitivity and Chemoresistance in Pancreatic Cancer. *Eur. J. Pharmacol.* 2014, 741, 8-16.
99. Schulze, H.; Kolter, T.; Sandhoff, K. Principles of Lysosomal Membrane Degradation: Cellular Topology and Biochemistry of Lysosomal Lipid Degradation. *Biochimica et Biophysica Acta (BBA) - Molecular Cell Research* 2009, 1793, 674-683.
100. Liao, K.-H.; Lin, Y.-S.; Macosko, C. W.; Haynes, C. L. Cytotoxicity of Graphene Oxide and Graphene in Human Erythrocytes and Skin Fibroblasts. *ACS Appl. Mater. Interfaces* 2011, 3, 2607-2615.

Main text figures

Scheme 1

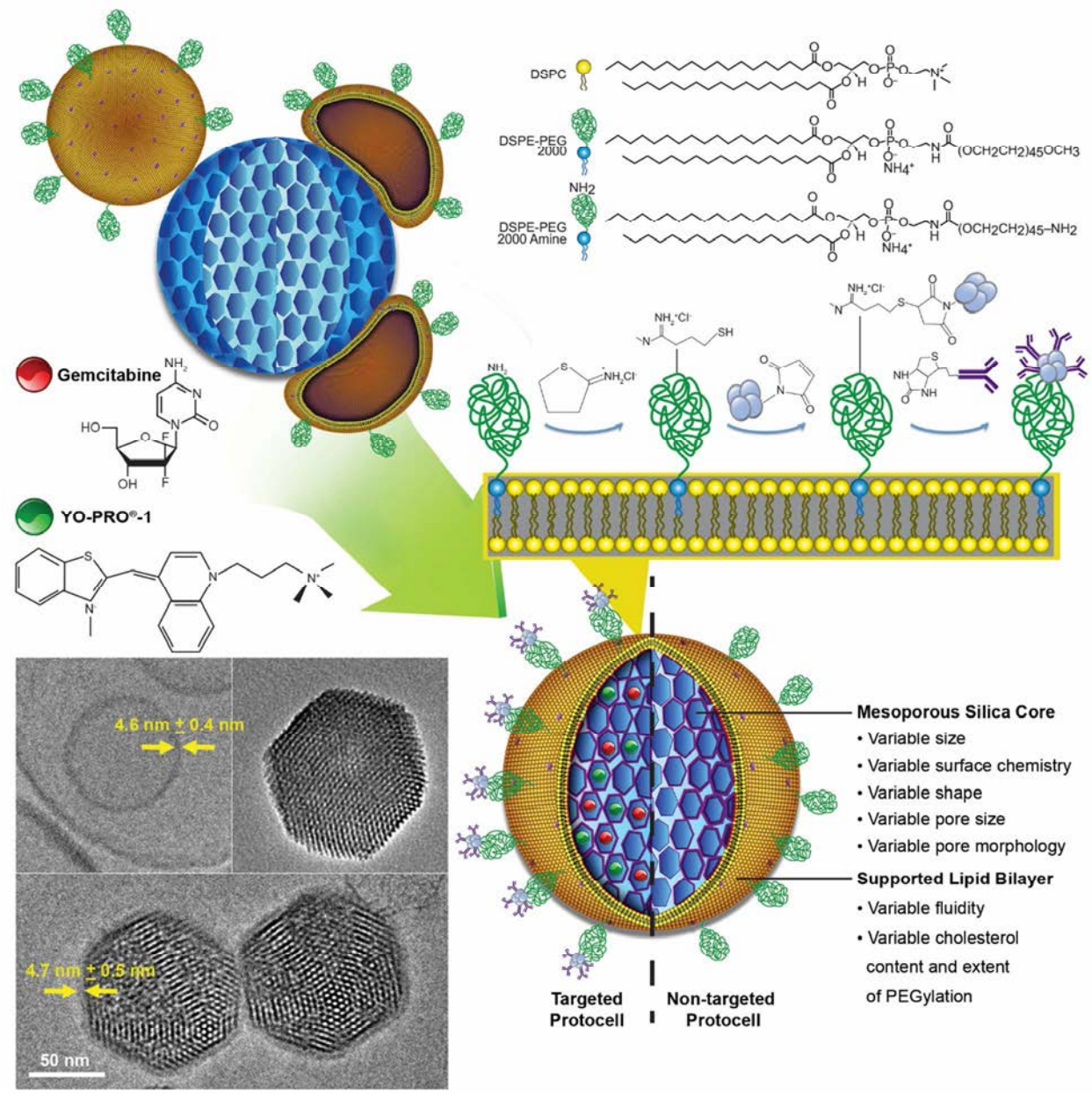

Scheme 1 – Schematic depicting lipid vesicle fusion onto monosized mesoporous silica nanoparticles (mMSN) to form mMSN-supported lipid bilayers (protocells). Drug (gemcitabine) and/or fluorescent molecular cargo (YO-PRO®-1) loaded protocells were assembled by soaking nanoparticle cores with cargo for 24h in aqueous buffer followed by fusion of (DSPC:chol:DSPE-PEG_{2000}-NH_2 – 49:49:2 mol ratio (targeted formulation) or (DSPC:chol:DSPE-PEG_{2000} – 54:44:2 mol ratio (non-targeted formulation) vesicles. Leukemia cell targeting was achieved by NeutrAvidin modification followed by binding to biotinylated EGFR antibodies. SLB thickness is nearly identical to that of the vesicle used for protocell synthesis as shown in cryogenic TEM images.

Figure 1

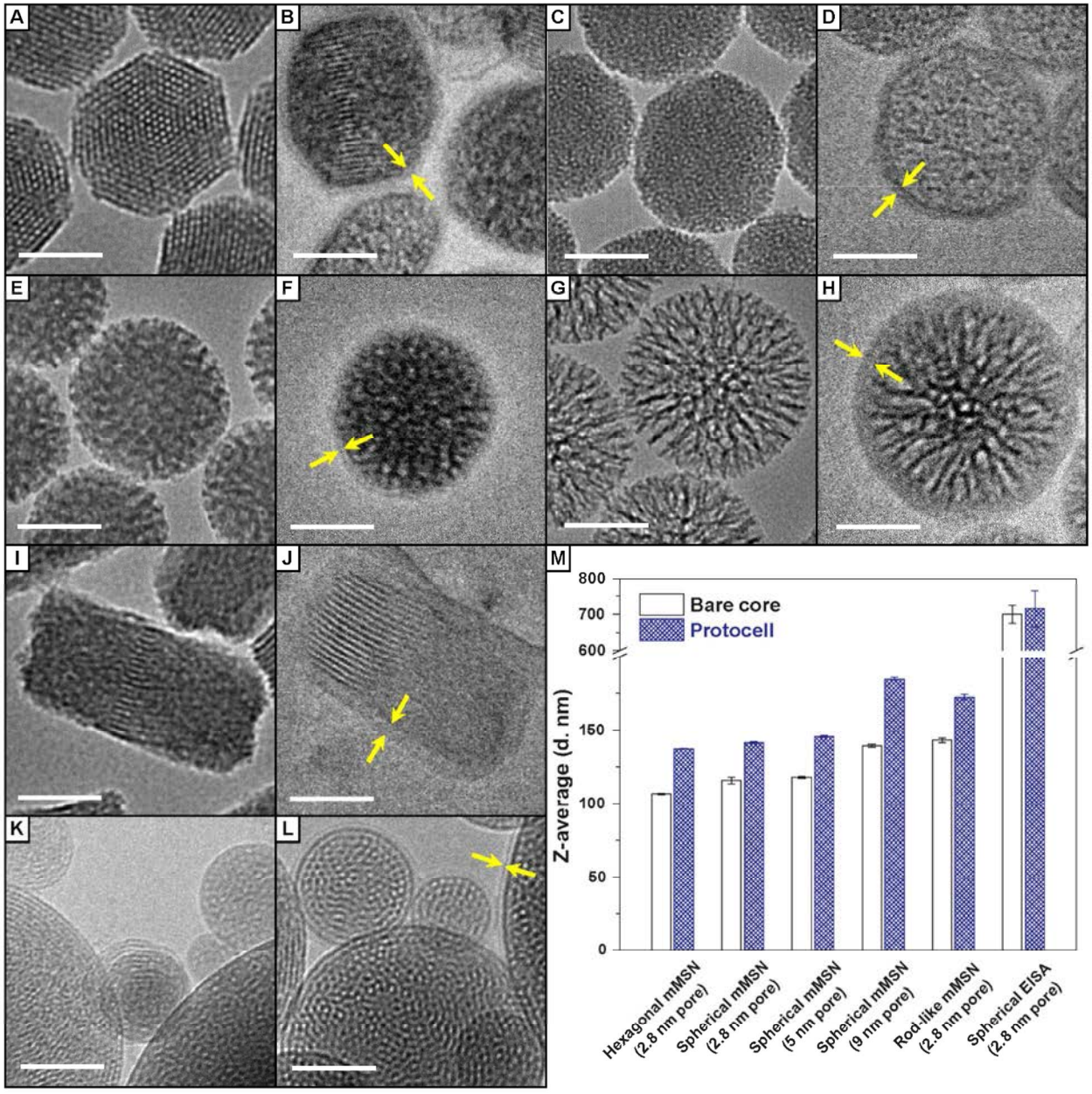

Figure 1 – Representative TEM and Cryo-TEM images of MSNs and corresponding protocells of various shape and pore morphology including (A and B) Hexagonal mMSNs and protocells, (C and D) Spherical 2.8 nm pore mMSNs and protocells, (E and F) Spherical 5 nm pore mMSNs and protocells, (G and H) Spherical 8 nm pore mMSNs and protocells, (I and J) Rod-like 2.8 nm pore mMSNs and protocells, (K and L) Aerosol assisted EISA MSNs and protocells. Yellow arrows highlight the SLB (~ 4.6 nm) in the Cryo-TEM images. (M) Hydrodynamic size analysis by DLS shows an increase in nanoparticle diameter following SLB fusion. DLS data represent mean ± SD, n=3. Scale bars = 50 nm.

Figure 2

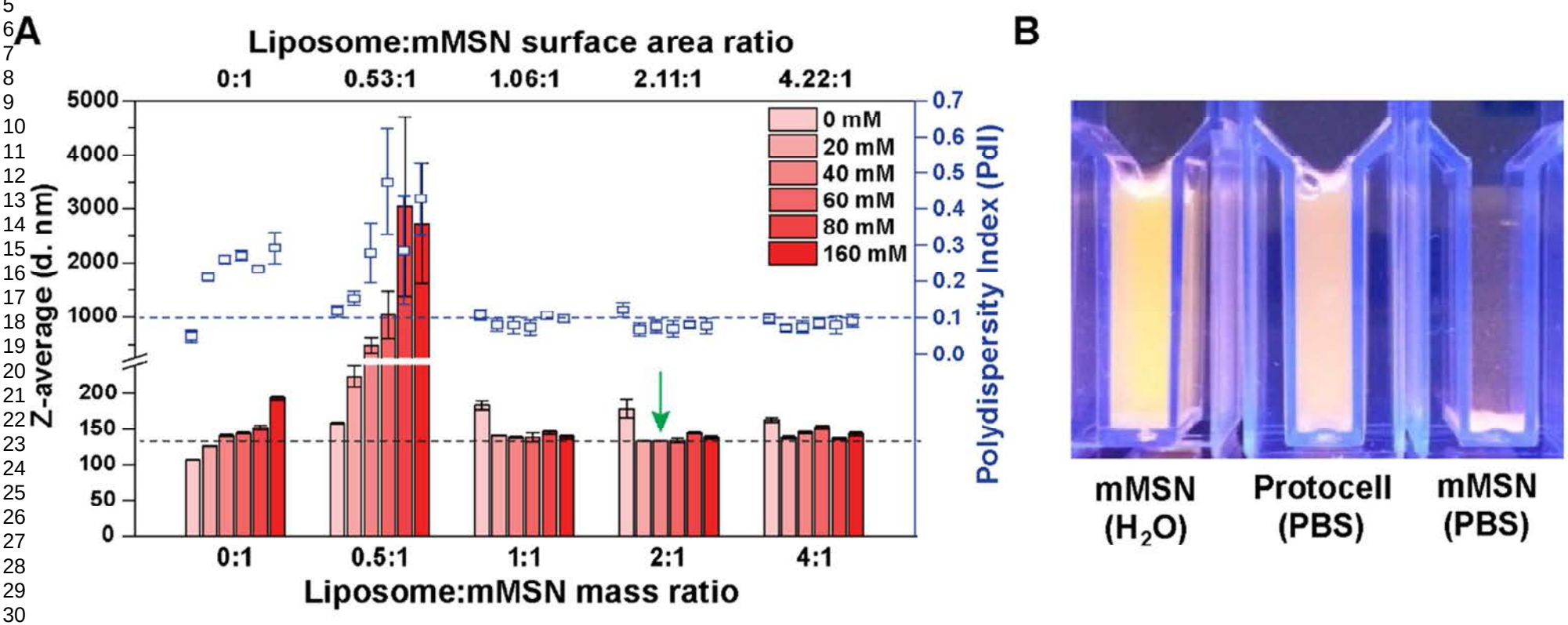

Figure 2 – (A) Comparison of Hexagonal protocells prepared in differing ionic strength conditions using different liposome to mMSN mass ratios (w:w) – bottom scale, and respective calculated inner liposome to outer mMSN surface area ratios – top scale. Hydrodynamic size (Left axis) corresponds to bar graph with black dashed line indicating optimal protocell size range. Polydispersity index (Right axis) corresponds to box plots with blue dashed line indicating threshold for monodispersity, values below the dashed line are considered monodisperse (PdI < 0.1). Green arrow identifies the optimal ionic strength and liposome:mMSN ratio fusion conditions used for subsequent experiments. (B) Fluorescentl mMSNs and protocells in cuvettes illustrate the colloidal stability of mMSNs in H_2O and aggregation driven settling of mMSNs in 160 mM PBS, protocells remain suspended in 160 mM PBS.

Table 1

Sample	Medium	Hydrodynamic Diameter (nm)	PdI	Zeta potential (mV)
mMSN	H_2O	106.90 ± 0.54	0.50 ± 0.015	-41.0 ± 0.9
mMSN	PBS	193.4 ± 2.83	0.292 ± 0.044	-28.1 ± 1.5
DSPC:chol:DSPE-PEG_{2000} Liposomes	PBS	92.54 ± 0.26	0.112 ± 0.006	-2.9 ± 0.8
Protocell	PBS	137.30 ± 0.30	0.085 ± 0.013	-3.3 ± 0.9

Table 1 – Hydrodynamic size characteristics and zeta potential measurements of modular protocell components. Liposome formulation DSPC:chol:DSPE-PEG_{2000} (mol % 54:44:2). Data represent mean ± SD, n=3.

Figure 3

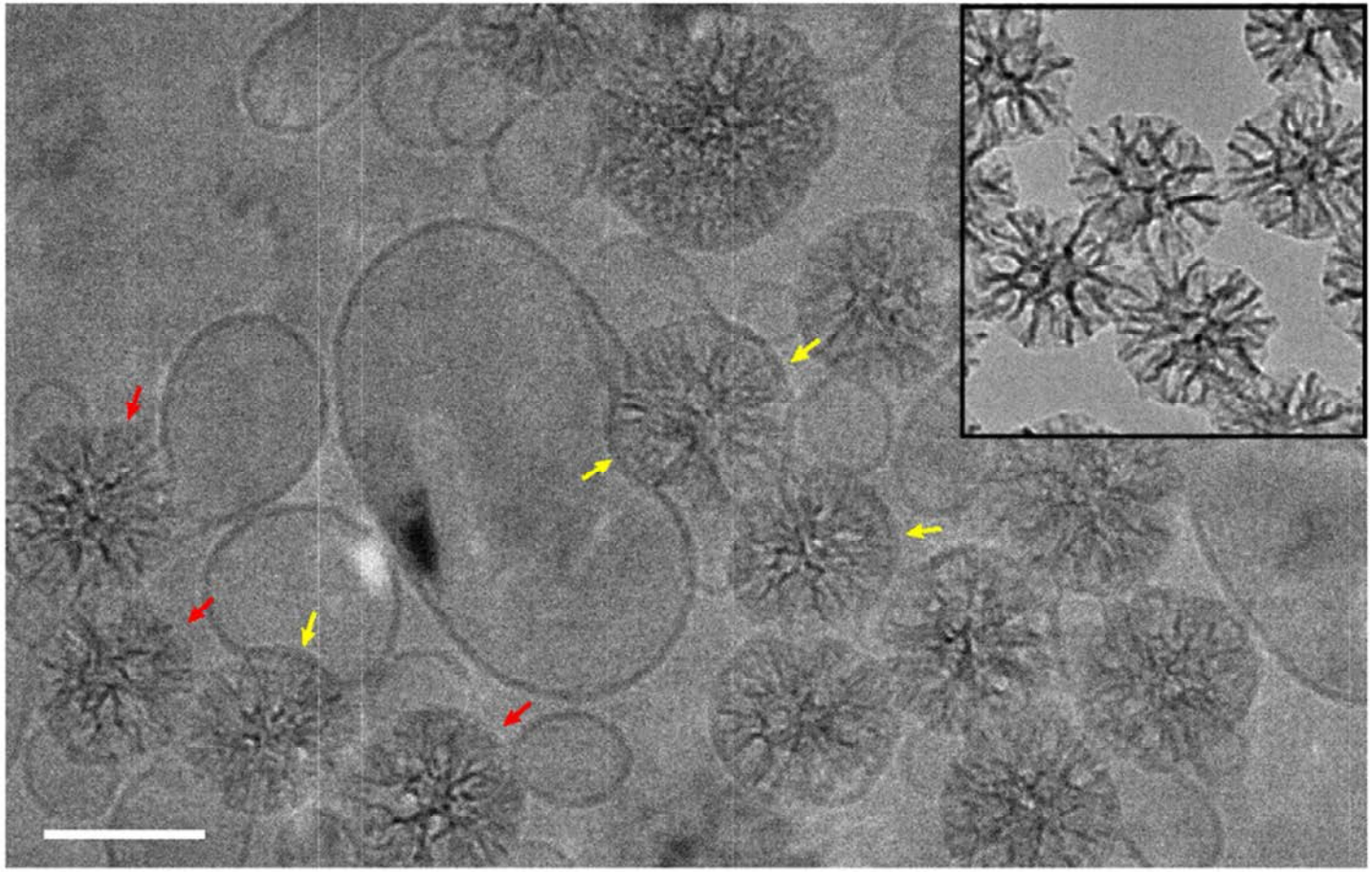

Figure 3 – Cryo-TEM image of 18 nm pore structured mMSNs mixed with liposomes under optimized fusion conditions as established in Fig. 2 showing large lipid-associated aggregates. (Inset): conventional TEM of 18 nm pore structured mMSNs. Yellow arrows highlight regions of liposome to silica interactions, red arrows highlight exposed silica surfaces. Scale bar = 100 nm. Corresponding hydrodynamic size measurements: mMSNs with 18 nm pore diameter, Z-average diameter = 123.0 ± 0.3 nm (Avg PdI = 0.056 ± 0.018); lipid associated aggregates Z-average diameter = 396.9 ± 13.0 nm (Avg PdI = 0.139 ± 0.043). DLS data represent mean ± SD, n = 3

Figure 4

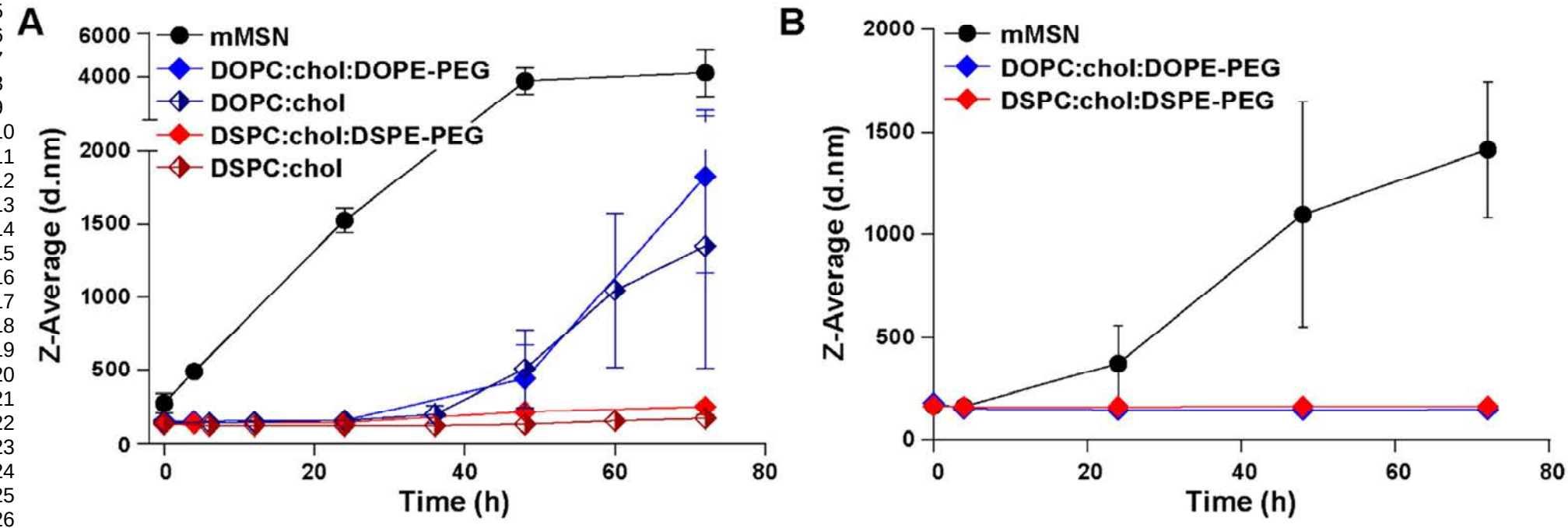

Figure 4 – (A) Hydrodynamic size of protocells prepared with differing SLB formulations *versus* incubation time at 37°C in 160 mM PBS. Trend in size change appears dependent on the extent of saturation of the lipid component of the SLB rather than PEGylation. (B) Hydrodynamic size of PEGylated protocells prepared with differing SLB formulations *versus* incubation time at 37°C in DMEM + 10% FBS. All data represent mean ± SD, n=3.

Figure 5

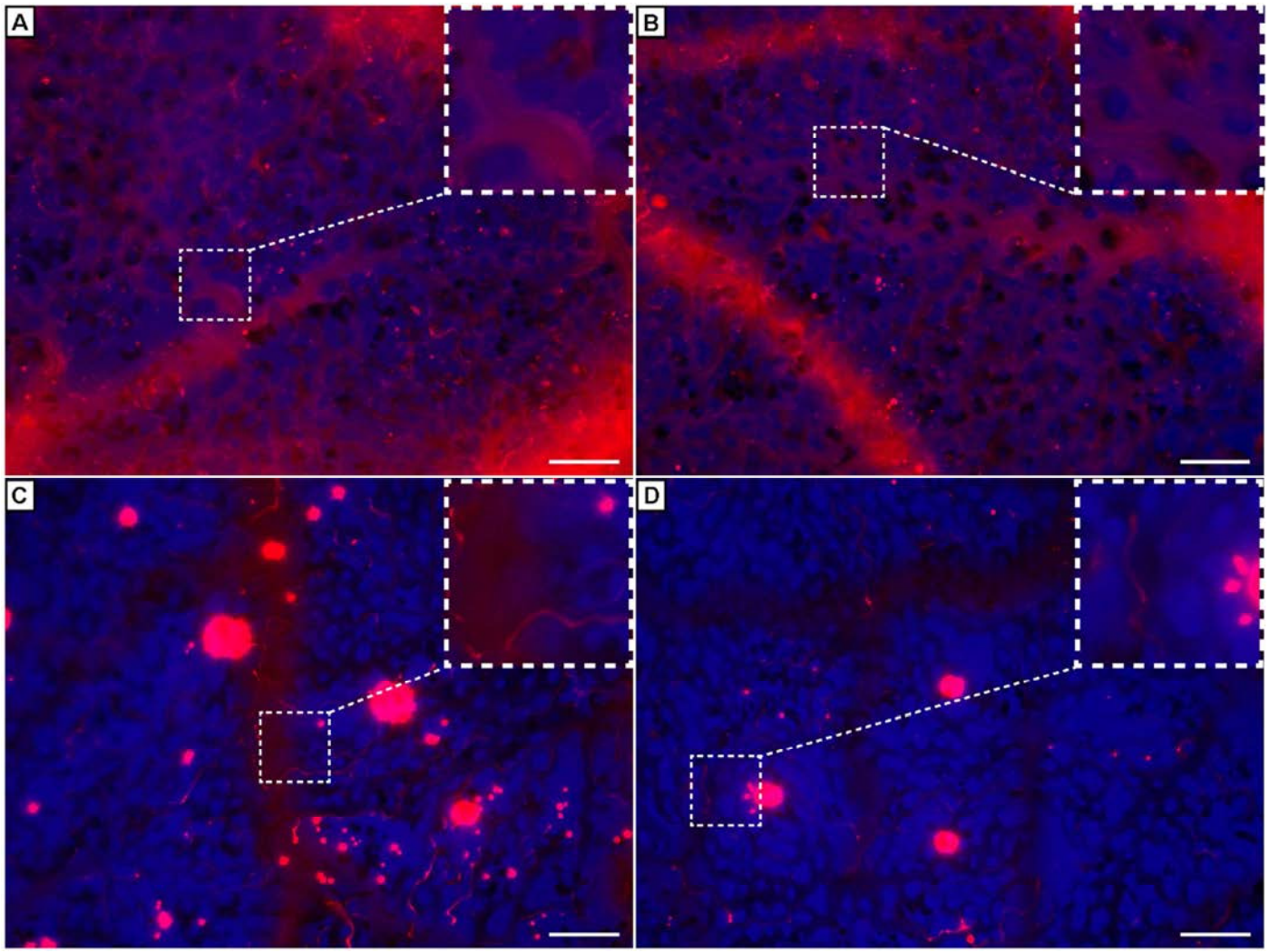

Figure 5 – Fluorescentl nanoparticle flow patterns observed using *ex ovo* CAM model. Representative panels highlight differential flow characteristics between (A) monosized protocells 5 minutes post injection and (B) 30 minutes post injection compared to (C) EISA protocells 5 minutes post injection and (D) 30 minutes post injection. Scale bar = 50 μm.

Figure 6

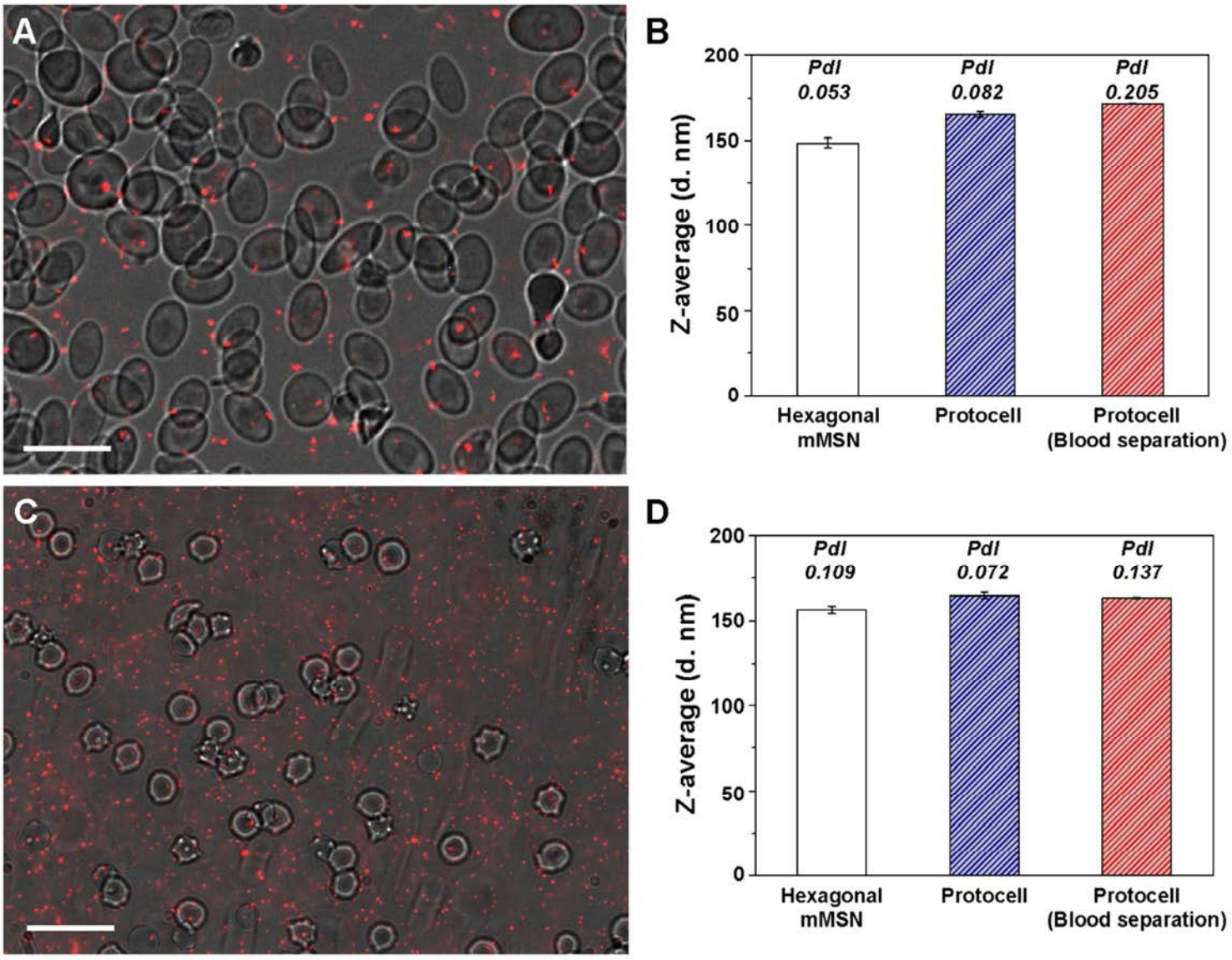

Figure 6 – (A) Red fluorescent protocells extracted from CAM 10 minutes post-injection and imaged on glass slide with Zeiss AxioExaminer upright microscope. We observed protocells in motion moving in and out of frame in a Brownian pattern with no apparent direct association with red blood cells. (B) Hydrodynamic size and PdI of core Hexagonal mMSNs, protocells, and protocells separated from CAM blood. (C) Fluorescent protocells injected and pulled from Balb/c mouse 10 minutes post-injection. (D) Hydrodynamic size and PdI of core Hexagonal mMSNs, protocells, and protocells separated from mouse blood. Injected protocells were separated from blood by variable speed centrifugation. Microscopy image scale bars = 20 μm and DLS data represent mean ± SD, n=3. Data provides evidence of size stability (A and B) *ex ovo* and (C and D) *in vivo* as assessed by minimal change in hydrodynamic size and PdI values.

Figure 7

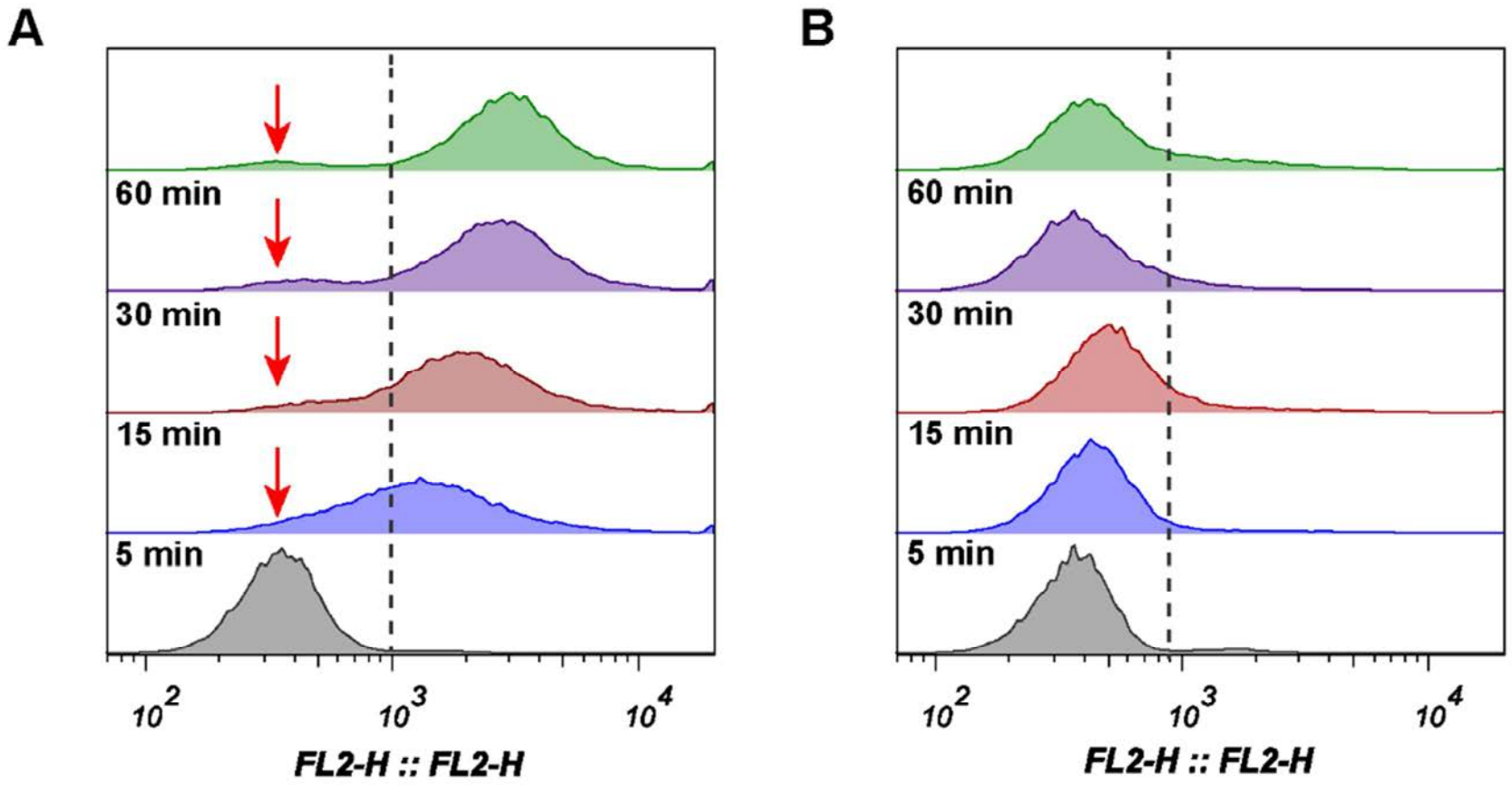

Figure 7 Flow cytometry analysis of REH-EGFR (A) and parental REH (B) cells incubated with red fluorescent EGFR targeted protocells at multiple time points. This data illustrates rapid specific *in vitro* protocell binding to REH-EGFR in as little as 5 minutes in complete medium, and maximal protocell accumulation after 30 minutes (A). Red arrows highlight non-EGFR expressing population of the engineered REH-EGFR cell line. There is minimal non-specific binding to parental REH cells (B).

Figure 8

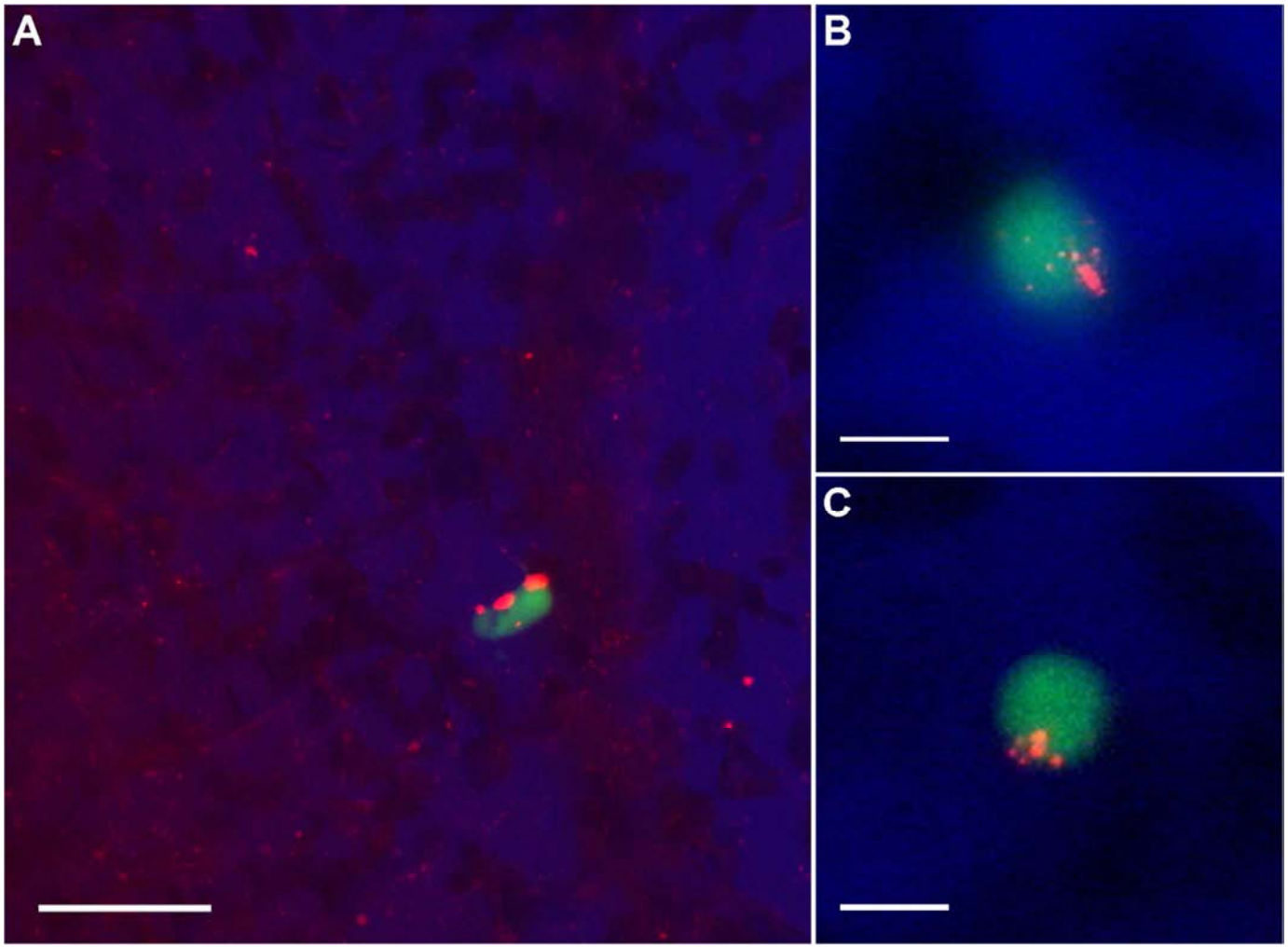

Figure 8 – Intravital fluorescent microscopy images acquired *ex ovo* in the CAM model reveal stable circulation of EGFR targeted protocells (red) and binding to REH-EGFR cells (green) in circulation at (A) 1 h, (B) 4 h, and (C) 9 h time points. Systemic protocell circulation is diminished after 4 h, however protocells remain associated with target cells for up to 9 h. Scale bar (A) = 50 μm, Scale bars (B and C) = 10 μm.

Figure 9

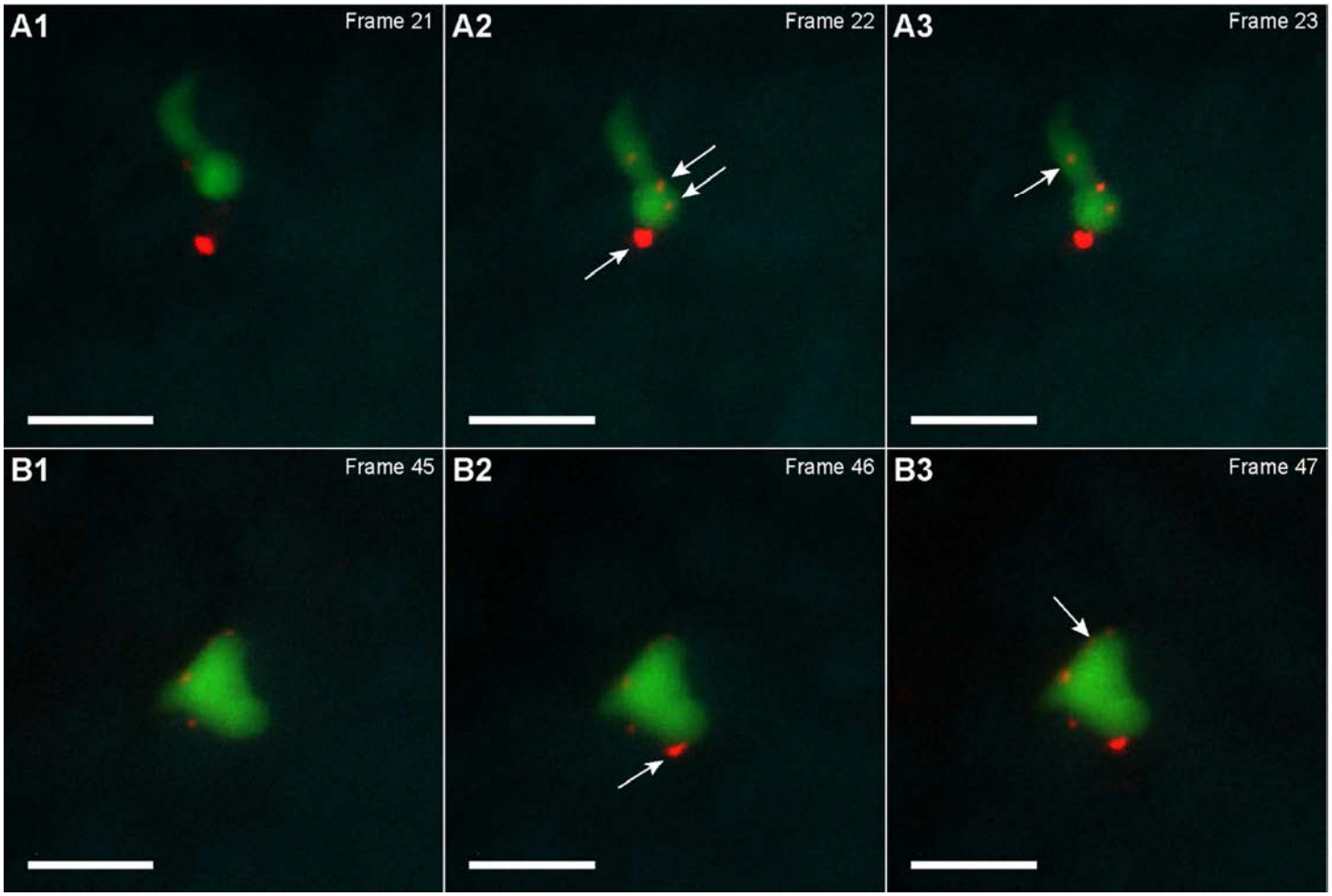

Figure 9 – Still frames which capture red fluorescent targeted protocell binding to green fluorescent labeled REH-EGFR cells captured in successive frames from Video S2 with arrows indicating points where red fluorescent protocells appear to bind and remain associated with the cells. Frame rate = 4.35 seconds. Scale bar = 20 μm.

Figure 10

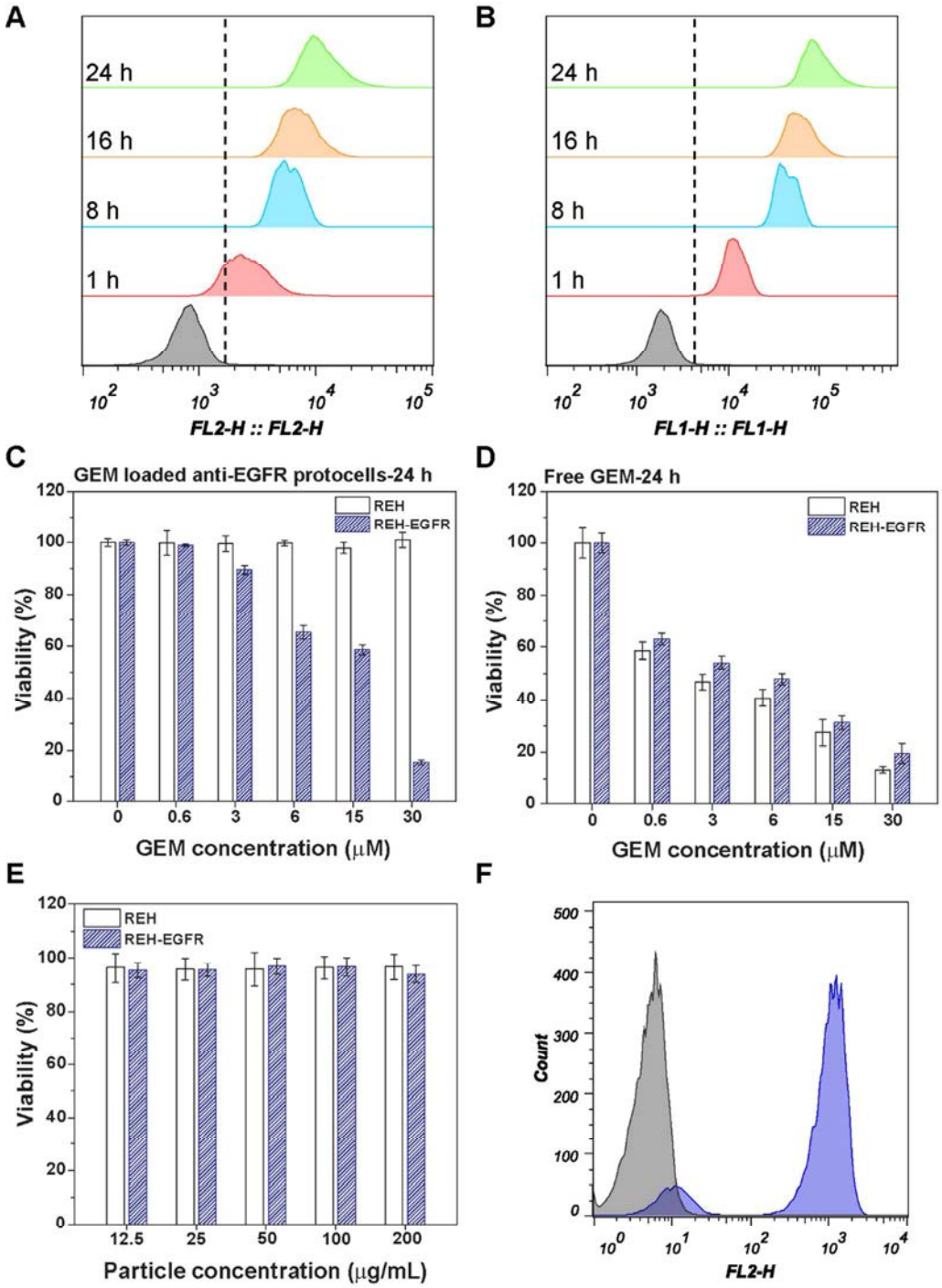

Figure 10 – Flow cytometry analysis to assess internalization of (A) red fluorescent EGFR-targeted protocells by REH-EGFR cells *in vitro* at multiple time points and (B) delivery of model drug, YO-PRO®-1, a green cell impermeant dye. After each time point, cells were acid washed to strip surface bound protocells then fixed. These data show an increase in the internalization of protocells and release of cargo with increasing incubation time. (C) Maintained viability of REH

cells and decrease in viability of REH-EGFR cells with increasing concentration of GEM loaded EGFR-targeted protocells. REH and REH-EGFR cells incubated with protocells from 0 to 50 ug/ml for 1 h, then washed to remove unbound protocells. Viability was assessed at 24 h. (D) Loss in cell viability of REH and REH-EGFR cells with exposure to increasing concentration of free GEM. Both cell lines were incubated with free GEM from 0 to 30 uM for 1 h, then washed to remove unassociated free drug. Viability was assessed at 24 h. Viability data highlights target specific delivery of cytotoxic cargo using monosized protocell platform and the non-specific cytotoxicity of free drug under the same conditions. (E) Cell viability of parental REH and REH-EGFR cells incubated with increasing concentrations of cargo-free anti-EGFR protocells for 1 h followed by washing to remove unbound protocells. Viability was assessed at 24 h. Viability data supports the biocompatibility of the monosized protocell platform. (F) Flow cytometry analysis of the EFGR expression of REH-EGFR cells as detected by binding of a PE-conjugated anti-EGFR antibody. Right-shifted histogram (blue) shows a majority of the population to be expressing EGFR. However, a minority population does not shift corresponding probably to REH-EGFR cells that have lost EGFR expression. Viability data represents mean ± SD, n = 3.

Figure 11

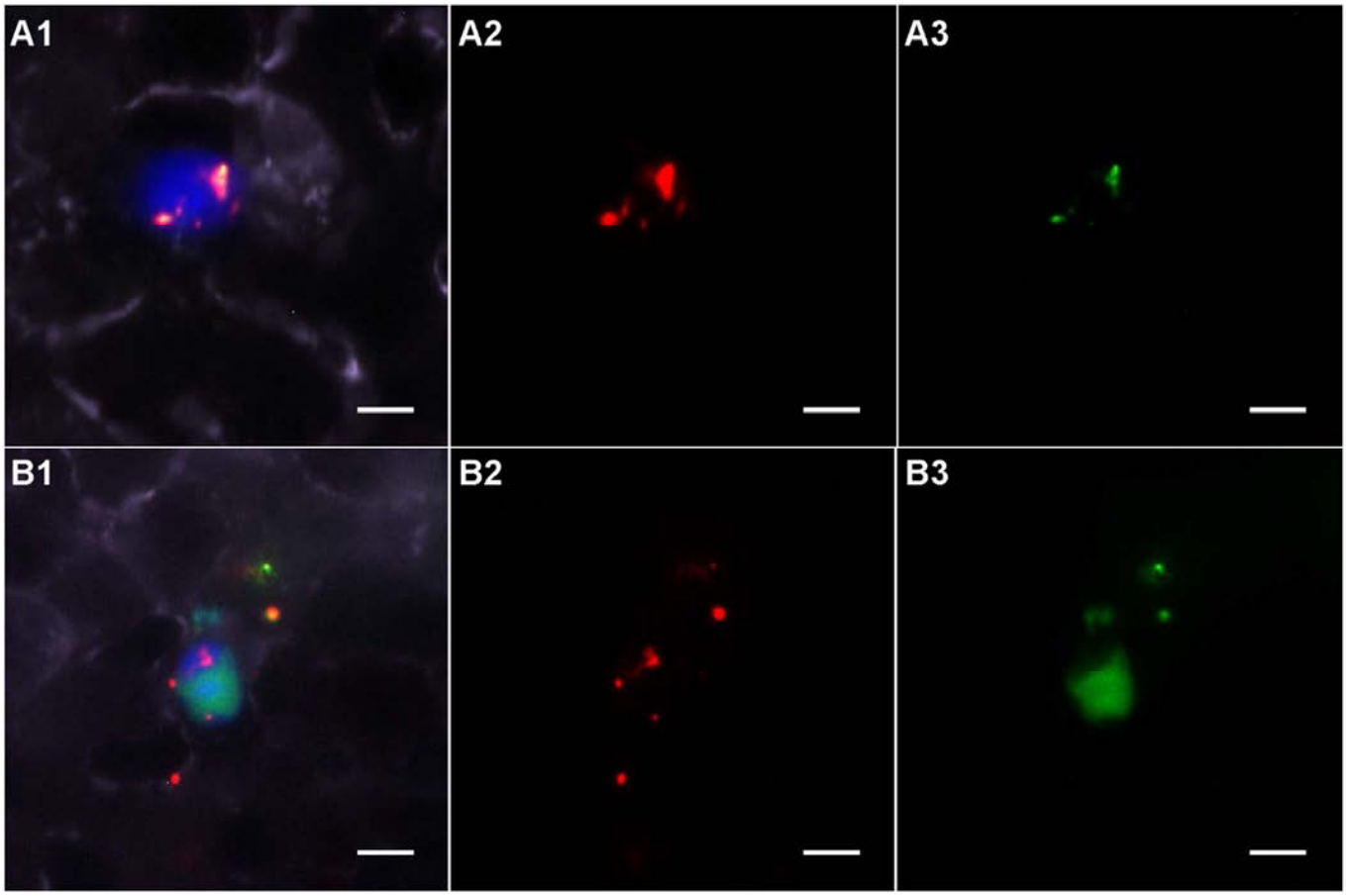

Figure 11 – Intravital fluorescent microscopy images acquired *ex ovo* in the CAM model showing green YO-PRO®-1 cell impermeant cargo loaded, red fluorescent EGFR-targeted protocells binding to and releasing cargo within REH-EGFR cells in a live animal model. (A1) Fluorescent overlay of (blue) REH-EGFR cell, (red) protocell, (green) YO-PRO®-1 cargo, (lavender) lectin vascular stain at 4 h post injection. (A2) Red channel shows protocell fluorescence, and (A3) green channel shows YO-PRO®-1 fluorescence associated with the protocells. However, after 16 h, (B1) fluorescent overlay shows release of YO-PRO®-1 cargo within the cell. (B2) Red channel shows 16 h protocell fluorescence and (B3) green channel shows YO-PRO®-1 release into the cell. Images acquired at 63x magnification, Scale bar = 5 μm.